The Dissertation Committee for Rongxin Huang

certifies that this is the approved version of the following dissertation:

Brownian Motion at Fast Time Scales and Thermal Noise Imaging

Committee:

Ernst-Ludwig Florin, Supervisor

Jack B. Swift

Wolfgang Frey

Michael C. Downer

Tomio Y. Petrosky

Brownian Motion at Fast Time Scales and Thermal Noise Imaging

by

Rongxin Huang, B.S.

Dissertation

Presented to the Faculty of the Graduate School of

The University of Texas at Austin

in Partial Fulfillment

of the Requirements

for the Degree of

Doctor of Philosophy

The University of Texas at Austin

December 2008

This dissertation is dedicated to my wife HongLiang for her help and encouragement during my graduate study, to our two little sons ShiGe and ShiDi, for their heavenly given smiles and to my parents BingShan and YiBin, brother RongTe and sister YaoTang, who define the meaning of a family and have given me endless love and support through my pursuit of a Ph.D.

Acknowledgments

First I would like to thank my advisor Prof. Ernst-Ludwig Florin for his continuous interest, encouragement, support and help in this work. EL is always full of ideas and curiosity, and he is also very thoughtful and inspiring. I have enjoyed every discussion we have over the past 4 years. I've also learned a lot from his interest-driven research style, which has made sometimes lengthy experiments more fun. I am also grateful to all my committee members for their generous encouragement and patience.

There are many people who have provided assistance with the experiments. Alexandr Jonas (Sasa) was a postdoc when I first joined the group. He was very knowledgeable and willing to help. I learned a lot from him about theories of optical trapping and instrumentation. Sasa also helped me in the designs of the photonic force microscope which later becomes the major instrument for all my experiments. Francesco Pampaloni gave me a lot of helpful suggestions regarding the alignment of the photonic force microscope. Christian Tischer was very helpful when I first started thermal noise imaging. Discussions with Branimir Lukic and Sylvia Jeney helped me get to the key problems quickly when we began to work on fast Brownian motion. Isaac Chavez and Prof. Mark Raizen were our collaborators on the fast Brownian motion project. Without their input and work on the fast position-positive detector, this work would not be possible. Isaac also participated in a majority of the experiments on the fast Brownian motion project, providing lots of helps in the

detector construction, machine shop work and data acquisition.

In general, I also learned a lot in discussions with many group members including Katja Taute, Pinyu Wu etc. I would like to thank all the members in the Biophysics group for making our lab friendly and fun. I also owe a debt to all the members of the Center for Nonlinear Dynamics for creating such a nice environment in which to work. I am grateful to our administrative support staff at CNLD, Olga Vera, Elena Simmons (who left CNLD last year) and Vanessa Munoz for helping me with tedious paperwork. I would also like to thank all members in the machine shop for producing nice mechanical parts for my experiments. My thanks also go to my good friend Donald Castiglioni for his critical reading on this manuscript.

Finally, I would definitely like to thank my parents, Bingshan and Yibin, and my wife Hongliang and all family members for their continuous trust and support. Without them, I could never make it this far.

Rongxin Huang

The University of Texas at Austin

December 2008

Brownian Motion at Fast Time Scales and Thermal Noise Imaging

Publication No. _____

Rongxin Huang, Ph.D.
The University of Texas at Austin, 2008

Supervisor: Ernst-Ludwig Florin

This dissertation presents experimental studies on Brownian motion at fast time scales, as well as our recent developments in Thermal Noise Imaging which uses thermal motions of microscopic particles for spatial imaging. As thermal motions become increasingly important in the studies of soft condensed matters, the study of Brownian motion is not only of fundamental scientific interest but also has practical applications.

Optical tweezers with a fast position-sensitive detector provide high spatial and temporal resolution to study Brownian motion at fast time scales. A novel high bandwidth detector was developed with a temporal resolution of 30 ns and a spatial resolution of 1 Å. With this high bandwidth detector, Brownian motion of a single

particle confined in an optical trap was observed at the time scale of the ballistic regime. The hydrodynamic memory effect was fully studied with polystyrene particles of different sizes. We found that the mean square displacements of different sized polystyrene particles collapse into one master curve which is determined by the characteristic time scale of the fluid inertia effect. The particle's inertia effect was shown for particles of the same size but different densities. For the first time the velocity autocorrelation function for a single particle was shown. We found excellent agreement between our experiments and the hydrodynamic theories that take into account the fluid inertia effect.

Brownian motion of a colloidal particle can be used to probe three-dimensional nano structures. This so-called thermal noise imaging (TNI) has been very successful in imaging polymer networks with a resolution of 10 nm. However, TNI is not efficient at micrometer scale scanning since a great portion of image acquisition time is wasted on large vacant volume within polymer networks. Therefore, we invented a method to improve the efficiency of large scale scanning by combining traditional point-to-point scanning to explore large vacant space with thermal noise imaging at the proximity of the object. This method increased the efficiency of thermal noise imaging by more than 40 times. This development should promote wider applications of thermal noise imaging in the studies of soft materials and biological systems.

Contents

List of Tables

List of Figures

Chapter 1

Introduction

The term *Brownian motion* is commonly used to refer to the physical phenomenon of microscopic particles moving about randomly in a fluid suspension. The fundamental aspect of Brownian motion is viewed as a simple stochastic process in a continuous domain that is indeed very common in nature. Examples include the stock market and exchange rate fluctuations, the evolution of physical characteristics in the fossil record and random terrains on the earth surface etc.

Brownian motion is named after botanist Robert Brown who systematically studied the erratic motions of pollen grains in water in 1827. The origin of Brownian motion remained unclear until the beginning of the 20^{th} century when the atomic nature of matter was still a controversial idea. Einstein and Smoluchowski observed that molecules of water would move at random if the kinetic theory of fluids was correct. Therefore, a small particle would receive a random number of impacts distributed with random strength and directions in any short period of time. This random bombardment by the molecules of the fluid would cause a microscopic particle to move in exactly the way described by Brown. A few years later, Perrin's

experimental observations on Brownian motion confirmed Einstein's theoretical results, and finally put an end to the two thousand year-old dispute about the reality of atom.

One of the important results of Einstein's theory is the Stokes-Einstein relationship, which relates the diffusion constant of the microscopic particle to a macroscopic parameter of the fluid – the viscosity. This relationship indicates that the properties of the fluid could be learned from the thermal motions of a Brownian particle embedded in the fluid. This remarkable result became the theoretical foundation of broad applications that use thermal motion to probe the properties of complex fluids or soft materials, such as emulsions, polymer networks or living cells.

However, Einstein's theory was not the final words on Brownian motion. As Einstein pointed out, his assumption of the statistically independent displacements of the particle in non-overlapping time intervals would break down at very short times. Brownian motion at fast time scales is dominated by the inertias of the particle and its surrounding fluids, as opposed to the common view that Brownian motion is completely random. The inertia effect of the particle is obvious. The remaining question is at what time scale it becomes apparent and how to observe it. The fluid inertia effect is more complicated and often overlooked in the study of Brownian motion. When the particle moves in the fluid, it will also disturb its surrounding fluid. Flow patterns are generated by the Brownian particle and propagate in the fluid, which can then act back on the particle at a later time. Brownian motion at fast time scales is very interesting, but experimental investigations have never been successfully achieved due to the lack of appropriate instrumentation ever since Brownian motion was discovered 180 years ago.

Colloidal particles whose size is on the order of one micrometer provide an im-

portant model system for studying Brownian motion. To observe Brownian motion at fast time scales requires a combination of high spatial and temporal resolution of the instrument. For example, a typical 1 μm sized colloidal particle in water moves about 1 nm within 1 μs at room temperature. Conventional techniques used to observe motions of colloidal particles include video microscopy and diffusing wave spectroscopy. In video microscopy, successive images of one or more colloidal particles are taken within a time interval of milliseconds, and centroid fitting algorithms are applied to track the particle's position with nanometer resolution. Diffusing wave spectroscopy can study the average Brownian motion of an ensemble of particles suspended in the fluid at the time scale of a microsecond. Due to its requirements of a large number of scattering events for each photon passing through the sample, a highly concentrated particle solution is needed. This results in strong hydrodynamic interactions between neighbor particles, which makes the interpretation of the data in diffusing wave spectroscopy difficult. Therefore, the quest to studying the inertia effect on Brownian motion requires a means to observe the motions on single particles with high spatiotemporal resolution, which cannot be achieved using neither video microscopy nor diffusing wave spectroscopy.

Optical tweezers which implement a high spatiotemporal resolution detector (photonic force microscope or PFM) provide an ideal solution for studying the Brownian motion at fast time scales. Since their invention in 1986, optical tweezers have found broad applications ranging from simple manipulations of microscopic objects to precise measurements of piconewton forces and nanometer or smaller displacements in biological systems etc. In optical trapping, a colloidal particle is confined at the focus spot of a laser beam. Due to the weak light-matter interaction, the thermal motions of the trapped particle is still significant with an amplitude rang-

ing from several tens of nanometers to a few hundred nanometers. At fast time scales, the influence of the optical force on the motions of the trapped particle is considered negligible compared to the thermal forces. Laser interferometry using forward scattered light from the particle and unscattered light provides a method to detect the Brownian motion of the trapped particle with high spatial and temporal resolutions. In this case, the PFM helps to maintain an isolated Brownian particle in the observation area for high resolution detection.

The observation of Brownian motion at short time scales is also of general interest in nanoscale science. Examples include the studies of diffusion of molecules within a complex environment e.g. a living cell, mechanical properties of single biopolymers and protein folding, where events happening at the nanometer scales are crucial.

In the rest of the dissertation, Chapter 2 presents the physical principles of optical trapping and three-dimensional position detection using laser interferometry, as well as the setup of the PFM and its characterization. This should help explain how the PFM works and why it is crucial for our experiments.

Chapter 3 reviews the theories of Brownian motion and different solutions to the Langevin equation that are relevant to our experiments. Experimental results demonstrating the inertia effects of particle and its surrounding fluid are discussed. Finally, the velocity autocorrelation function of a Brownian particle is obtained and its good agreement with theory to the ballistic time scale is shown.

Chapter 4 presents our development of thermal noise imaging as an example of using Brownian motion as a natural scanner. An efficient imaging strategy is described which facilitates the applications of thermal noise imaging to large scale objects.

The last chapter contains a summary of this work.

Chapter 2

Development of Photonic Force Microscope

Photonic Force Micrscope (PFM) is essentially optical tweezers implemented with fast and high resolution three-dimensional single particle tracking. Its aims are to have similar applications as atomic force microscope, e.g. force measurements and profile imaging. Since all experiments throughout this dissertation were performed in a PFM, an introduction to optical trapping and three-dimensional single particle tracking using laser interferometry is helpful. This chapter begins with a review of the developments of optical trapping and its broad applications in physical and biological science. Physical principles of optical trapping are explained. General requirements and the setup of the PFM are discussed. Calibration of the PFM and correction for nonlinearity in position signals are presented at the end of the chapter.

2.1 Historical review

Light carries linear and angular momentum so that it can exert forces and torques on physical objects. The first observed evidence of the radiation pressure of light dates back to four hundred years ago when the famous astronomer Johannes Kepler observed that the tail of comets always point away from the sun, which he thought might be due to some kind of solar pressure. As we now know a photon's momentum is so small, besides extraterrestrial experiments, the effect of radiation pressure was rarely observed before the advent of the laser in the 1960s [1, 2]. A laser provides high intensity coherent photons, making the effect of radiation pressure observable in the lab when the laser impinges on microscopic particles [3].

In 1970, Arthur Ashkin first demonstrated that the radiation pressure from a focused laser beam could accelerate and decelerate small micrometer sized latex particles [4]. In that experiment, he also discovered that gradient forces resulting from the laser intensity gradient could draw the latex particle to the position of intensity maximum. In a series of papers [5–8], Ashkin later showed that radiation pressure could be used to levitate micron-sized particles in water or air, and a three-dimensional stable levitation trap could be achieved in vacuum. In 1986, Ashkin demonstrated that dielectric particles with sizes ranging from 25 nm to 10 μm can be trapped at the focus spot of a tightly-focused Gaussian beam [9]. This so-called single beam gradient trap (now termed "Optical Tweezers") became the most popular form of optical trapping ever since then due to its simple optical layout. Over nearly 20 years of development, optical tweezers have found many applications in scientific research, ranging from simple manipulations of microscopic objects to precise measurements of piconewton forces and nanometer or smaller displacements in biological systems, and three-dimensional thermal noise imaging

of polymer networks etc.

The manipulation of microscopic objects was the most direct application of optical tweezers when they were discovered to be able to trap micron-sized particles. This has been applied to different physical systems, including dielectric particles [9–17], metal particles [18], liquid droplets [19], viruses, bacteria and other types of cells [12, 20, 21]. To prevent photo damage or heat denaturation of biological samples, infrared laser was chosen over the initially-used green laser to minimize the absorptions from the biological materials and liquid medium [3]. With a power of 50 mW for a 1064 nm Nd:YAG infrared laser, motile bacteria could be confined within an optical trap for many minutes without causing apparent damage. Of course, the power thresholds for damaging biological materials are different for different samples with a typical range from 50 to 100 mW. To simultaneously manipulate multiple particles, time-share optical tweezers that use acousto-optic deflectors (AOD) or scanning mirrors to provide rapid deflection and switching of the trapping beam were applied to create arrays of trapping sites [22–24]. The use of AOD or scanning mirrors provides the ability to trap tens of particles simultaneously since they are able to switch the beam with a high frequency. The other alternative for creating multiple traps is to use a spatial light modulator (SLM) to generate holographic patterns that could trap particles at each intensity maximum or minimum position [25, 26]. Additionally, a Bessel beam has also been used to trap multiple particles at different planes along the optical axis [27, 28]. Bessel beam does not have strong divergence from the focal plane and it could also reconstruct itself after a characteristic propagation distance if the beam is obstructed or distorted by a trapped particle, which makes it a perfect candidate for trapping multiple particles along the optical axis. A combination of a Bessel laser beam and a SLM allows

for the creation of a lattice of optical traps in three dimensions. Using multiple traps in two or three dimensions has been extended to study particle dynamics on a washboard potential or phase transitions in colloidal crystals [29, 30].

When the position of the trapped particle can be monitored with high precision (by either video microscopy [31, 32] or laser interferometry with split photodiodes [33–35]), the particle becomes a sensitive sensor for measuring forces and position displacements when it is linked to biomolecules. Optical tweezers have been applied to measure the forces generated by mechanochemical enzymes such as molecular motors [36–39] and RNA polymerase [40–42], and the forces to unfold muscle proteins and RNA hairpins [43–45]. The recent developments of ultra-stable optical tweezers have also allowed for the direct observation of base-pair stepping by RNA polymerase [46], and following individual ribosomes as they translate single messenger RNA hairpins one codon at a time [47]. The capability of resolving finer forces and displacements would allow optical tweezers to have broader applications in investigating an increasing number of biochemical and biophysical processes.

Since optical tweezers can apply minimum forces at the same order of thermal forces, they become a powerful tool for studying many problems in thermodynamics. Brownian motions of optically trapped micron-sized colloidal particles in steady fluid flow have been used to study the violation of the second law of thermodynamics for small systems and short time scales [48]. Since optical tweezers can disturb a system under both thermal equilibrium and nonequilibrium conditions, it becomes possible for the first time to experimentally investigate various forms of the fluctuation theorem for non-equilibrium systems [49–51]. Reversible folding of nucleic acid hairpins using optical tweezers also allows us to construct the full shape of energy landscape and distinguish different sequences of nucleic acids [51, 52].

The amplitudes of thermal motion of an optically-trapped particle are significant, ranging from a few tens of nanometers to several hundred nanometers due to the weak light-matter interaction. Brownian motions of the trapped particle contain information about the trapping potential and the properties of the surrounding environment. With the advent of the fast position detection method using split photodiodes, Brownian motions of trapped particle was first used to calibrate the optical trap [53], and later applied to study the mechanical properties of kinesin motor proteins in three dimensions [54]. Brownian motions of the trapped particle can also be applied to image three-dimensional structures of polymer networks [55] which we will discuss in further detail in Chapter 4.

In short, optical tweezers have been established as a powerful technique spanning different fields and applying to different length scales, from single molecules to large cells. We should be able to see more applications of optical tweezers to physical and biological problems with improved spatiotemporal resolution and stability, and its combinations to other existing techniques.

2.2 Physical principles of Optical Tweezers

Theoretical modeling of optical tweezers can be readily achieved in two limiting cases: when the particle's size is greatly larger than the wavelength of laser, the conditions of Mie scattering are fulfilled, and the particle can be deemed as a simple lens and ray optics can be applied to calculate the forces; when the particle's size is significantly smaller than the wavelength, the particle is approximated as a point dipole and the theories of Rayleigh scattering apply.

Ray optics calculations of optical forces in Mie scattering regime (typically $a/\lambda > 10$, where λ is the wavelength of light and a is the radius of the particle) have

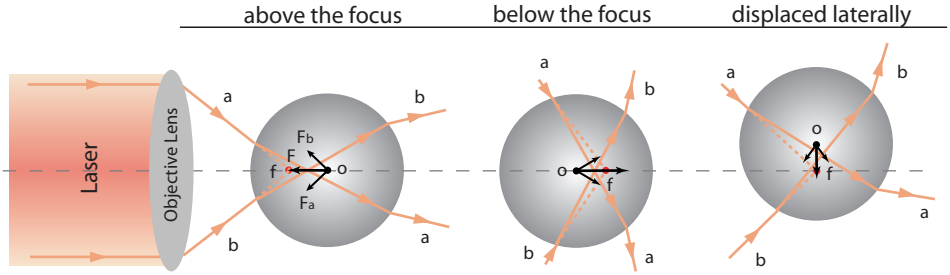

Figure 2.1: Qualitative view of the trapping of dielectric spheres by ray optics when the particle is above, below or displaced laterally from the geometric focus spot. f indicates the geometrical focus and o indicates the center of the particle. The refraction of a typical pair of rays a and b of the trapping beam gives forces F_a and F_b, which generates the total restoring force F for axial and transverse displacements from the trap focus.

been demonstrated by Ashkin in 1992 [56]. Figure 2.1 shows the qualitative view of three-dimensional trapping of dielectric spheres. Refraction of the incident light by the sphere corresponds to a change in the momentum carried by the light. An equal amount but opposite momentum changes would be imparted to the sphere after the light is refracted. As a result, the pair of rays a and b as shown in Figure 2.1 will give rise to F_a and F_b whose vector sum F is always restoring for axial and transverse displacements of the sphere from trap focus, thus forming a three-dimensional stable trap. Detailed calculations of optical forces in ray optics can be found in [56].

In Rayleigh regime where $\lambda/a > 10$, the electromagnetic field $\vec{E}(\vec{r}, t)$ of the light can be considered uniform over the entire particle. The particle can be assumed to be an induced simple point dipole. The radiation force exerted on this dipole can be naturally divided into two components: a scattering force component due to the scattering from the induced point dipole and a gradient force component due to the Lorentz force acting on this dipole. The induced dipole moment for a particle with

radius a and a dielectric constant ε_1 can be obtained as [57]:

$$\vec{p}(\vec{r},t) = 4\pi\varepsilon_0 a^3(\frac{\varepsilon_1-\varepsilon_2}{\varepsilon_1+2\varepsilon_2})\vec{E}(\vec{r},t) = 4\pi n_2^2\varepsilon_0 a^3(\frac{m^2-1}{m^2+2})\vec{E}(\vec{r},t) \tag{2.1}$$

where $m = n_1/n_2$ is the ratio of the refractive index of particle n_1 to that of liquid medium n_2, ε_0 and ε_2 are the dielectric constants of vacuum and liquid medium respectively.

Thus the instantaneous gradient force is given by

$$\vec{F}_{grad}(\vec{r},t) = [\vec{p}(\vec{r},t)\cdot\nabla]\vec{E}(\vec{r},t) \tag{2.2}$$

The steady state gradient force can be acquired by time-averaging of Equation (2.2)

$$\begin{aligned}\vec{F}_{grad}(\vec{r}) = \langle\vec{F}_{grad}(\vec{r},t)\rangle_T &= 4\pi n_2^2\varepsilon_0 a^3(\frac{m^2-1}{m^2+2})\frac{1}{2}\nabla\langle\vec{E}(\vec{r},t)^2\rangle_T \\ &= \pi n_2^2\varepsilon_0 a^3(\frac{m^2-1}{m^2+2})\nabla|\vec{E}(\vec{r})|^2 \\ &= 2\pi n_2^2\varepsilon_0 a^3(\frac{m^2-1}{m^2+2})\nabla I(\vec{r})\end{aligned} \tag{2.3}$$

Here we can see that the gradient force is proportional to the intensity gradient $\nabla I(\vec{r})$. Also for $m > 1$, the gradient force is pointing towards the intensity maximum. That's why latex particles in water are drawn to the focus spot of the laser beam while air bubbles are repelled from it.

The scattering force component is given as the following

$$\vec{F}_{scat}(\vec{r}) = \frac{C_{pr}\langle\vec{S}(\vec{r},t)\rangle_T}{c/n_2} = \hat{z}\frac{n_2}{c}C_{pr}I(\vec{r}) \tag{2.4}$$

where C_{pr} is the scattering cross section of the particle, $\hat{z}$ is the unit vector in the

beam propagation direction and c is the speed of light. C_{pr} is given by [58]

$$C_{pr} = \frac{8}{3}(\frac{2\pi a}{\lambda})^4 a^2 (\frac{m^2-1}{m^2+2})^2 \tag{2.5}$$

So the final form of the scattering force is given as

$$\vec{F}_{scat}(\vec{r}) = \hat{z}\frac{\sigma n_2}{c} I(\vec{r}) \tag{2.6}$$

where

$$\sigma = \frac{128\pi^5 a^6}{3\lambda^4}(\frac{m^2-1}{m^2+2})^2$$

Note that the scattering force always points toward the light propagation direction.

For the particle size falling into the intermediate regime where $\lambda \sim a$, which is often the case in optical trapping, neither Rayleigh theory nor ray optics calculation is a good approximation. More complete electromagnetic theories are required for an accurate description in this so-called Lorentz-Mie regime that is usually very difficult to model [59].

Apart from the above mentioned challenges, it is also generally difficult to model the exact trapping beam profile at the geometric focus spot. Parallel axis approximation would not correctly describe a tightly focused laser beam, so that higher-order corrections of the Gaussian beam have to be assumed for an accurate electromagnetic-field model. But even that would not completely reproduce the realistic incident-field distributions because of the influence of the objective lens aperture that cuts off a portion of the Gaussian beam and phase distortions like spherical aberrations [60].

So in real optical trapping experiments, the properties of the trap are acquired through calibration instead of from theoretical modelling. Theories of optical

trapping are helpful in providing a qualitative understanding of the trap.

2.3 Photonic Force Microscope setup, calibration and performance

2.3.1 Photonic Force Microscope setup

Since the trapped objects are all microscopic particles, the optical trap is usually incorporated into conventional light microscopes for visualization and manipulation. Figure 2.2 shows the schematic drawings of our photonic force microscope. In the following section we will explain requirements and functions of each component.

Optical trapping

As we know from the physical principles of optical trapping, light intensity gradients provide restoring gradient forces which is the key for a stable optical trap. Usually a Gaussian beam focused by a lens is used to create such a three-dimensional intensity gradient. Lateral intensity gradients are inherent in a Gaussian beam, while the gradient along the optical axis is achieved through focusing by the lens. A continuous wave Gaussian beam is usually used in practice although there have been few examples for optical trapping with a pulse laser [61]. In our setup, an infrared diode-pumped Nd:YAG laser (IRCL-850-1064-S, CrystaLaser USA) with a wavelength of $\lambda = 1064$ nm is used. This is a single longitudinal and TEM00 mode laser with a maximum output power of 850 mW. The power stability ($< 0.25\%$ over 24 hours) and pointing stability (± 0.02 mrad) is very good, which is critical to achieving a stable optical trap. Pointing instabilities will lead to unwanted fluctuations of the focus spot and thus the optical trap position, whereas power

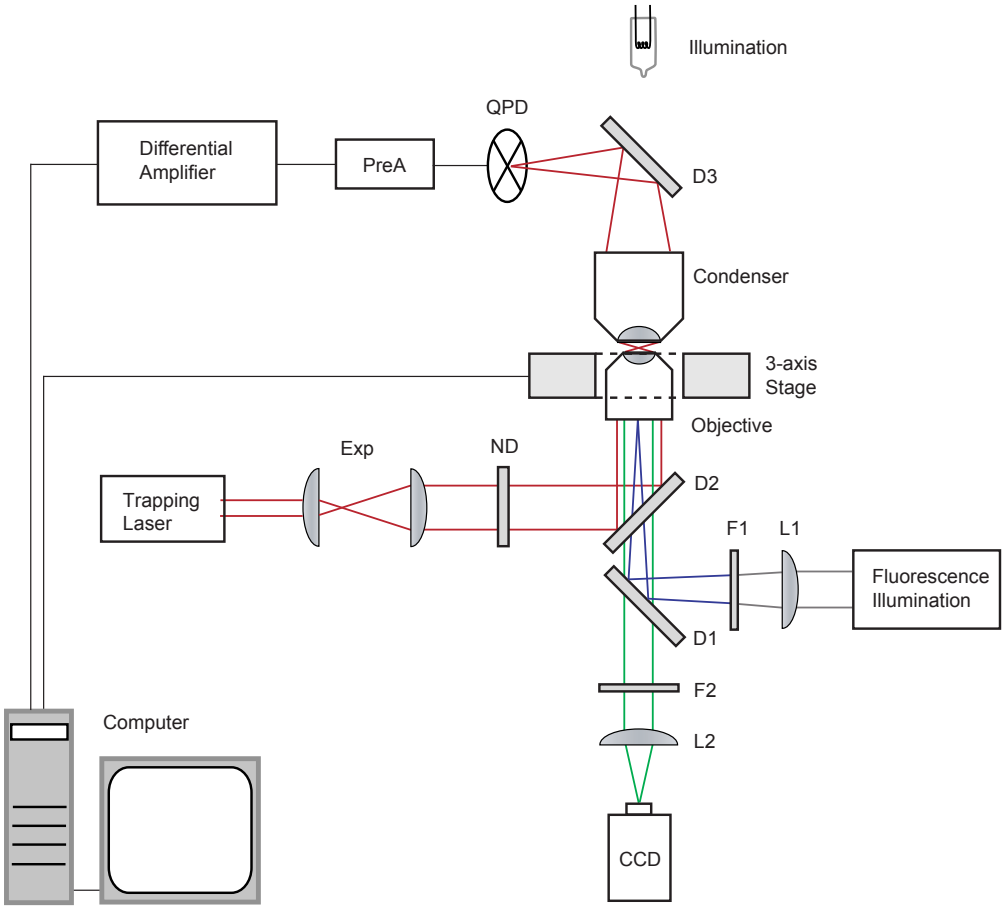

Figure 2.2: Sketch of Photonic Force Microscope. Exp: beam expander; D: dichroic mirror; F: filter; L: lens; ND: neutral density filter; QPD: quadrant photodiode; PreA: preamplifier.

fluctuations will lead to temporal variations in the spring constants of the optical trap. The beam diameter at $1/e^2$ is about 0.45 mm and has a divergence angle of 3.6 mrad. Immediately after the beam exits the laser housing, a 20X beam expander (S6ASS2320/126, SillOptics, Germany) is used to enlarged the beam to an appropriate size that would overfill the back aperture of the objective lens by a factor of about 2. Overfilling the back aperture of the objective lens is helpful for achieving a plane wavefront and a tight focus spot. A dichroic mirror D2 (950dcspuv-3p, Chroma Technology Corp, USA) is used to reflect the expanded laser beam into the objective lens. The dichroic mirror has a transmission coefficient of more than 90% at wavelength of 350-900 nm, and a reflection coefficient above 95% of wavelength greater than 1000 nm. To create strong gradient forces that can overcome the scattering forces, usually objective lenses with high numerical apertures are used. The diameter of the smallest focal point on a high numerical aperture lens is on the order of the laser wavelength. Our custom-designed platform can accept water- or oil-immersion objective lenses from both Olympus and Zeiss due to their same thread standards. Specifically, we used two different objective lenses for different experiments, a 63x water-immersion objective (UPlanSApo 60x/1.20W, Olympus, Japan, NA=1.2) and a 100x oil-immersion objective (Plan-NEOFLUAR 100x/1.30 Oil Pol, Zeiss, Germany). The water-immersion objective lens has a large working distance of 250 μm, which allows the trap to go deep into the sample chamber. Also, the water-immersion lens minimizes the refractive index mismatch between the immersion medium and the sample, which is known to be a problem for the oil-immersion lens [62]. On the other hand, the immersion oil evaporates much slower than water, which can minimize the temperature gradient and reduce the drift of the setup due to the evaporation of the immersion medium. To tune the stiffness of

the optical trap, neutral density filters can be placed right after the beam expander to adjust the laser powers.

Positioning of the sample

Nanopositioning of the optical trap in the sample chamber is achieved by a three-axis piezostage (P-561, Physik Instrumente, Germany). This piezostage has a maximum scanning range of 100 μm along lateral dimensions with a precision of 1 nm, and a maximum range of 50 μm along the optical axis with a precision of 0.5 nm. A digital controller (E-710, Physik Instrumente, Germany) hooked to the computer through GPIB interface is able to accept movement commands in nanometers and applied corresponding voltages to drive the piezostage. The sample chamber is tightly fixed on top of the piezostage and moved relative to the objective lens. The bottom of the piezostage is attached to an aluminum plate that has three legs with a 10 mm stainless steel sphere glued at the end of each leg. The legs stand on optically flat sapphire plates embedded on the microscope platform. Thus the entire stage is also moveable by hand for coarse positioning of the sample chamber.

Bright field and fluorescence imaging

The microscope also incorporates fluorescence microscopy and bright field microscopy to visualize the trapped particle. Bright field imaging is convenient to visualize particles with diameters larger than 500 nm, while fluorescent imaging is generally good for fluorescent particles of any size.

In fluorescent imaging, the fluorescence illumination is provided by a metal halide lamp that contains halogens (X-Cite 120, EXFO, Canada). The halogens prevent the deposition of carbon on the quartz walls of the lamp and extend the lifetime of lamp to a tremendous number of 1500 hours. Light coming out from

the lamp has been collimated so that an achromatic lens L1 with anti-reflection coating (Linos, USA, focal length=180 mm, diameter=40 mm) is used to focus the beam to the back focal plane of the objective, which can provide a homogeneous illumination of the sample. The wavelength of light emitting from the lamp ranges from 350 to 600 nm. A bandpass filter F1 is placed right after lens L1 to select a suitable excitation light for the flurophores. A dichroic mirror D1 is used to reflect the excitation light and allow the transmission of emission light from flurophores at longer wavelengths. Another bandpass filter F2 placed on the detection path allows only the transmission of emitted light from the flurophores. A tube lens L2 (Linos, USA, focal length=180 mm, diameter=40 mm) focuses the light into a CCD camera (Rolera-XR, QImaging, USA), allowing the acquisition of the fluorescence images.

For bright field illumination, the condenser (ACHROMATIC-APLANATIC CONDENSER 0.32 POL, Zeiss, Germany) collects and shines the light from a LED lamp onto the sample. The light transmitting through the sample is collected by the objective lens, and focused by the same tube lens L2 to the CCD camera.

Control of vibration and air flow

To minimize mechanical vibrations transmitted from the building, the entire PFM is built on top of an optical table with tuned damping (RS-4000, Newport, USA), supported by pneumatic isolators (I-2000, Newport, USA). The table is floated with high pressure nitrogen gas. To adjust the load distribution on the table, additional lead blocks with different weights can be placed on the table at appropriate places to achieve an efficient damping.

Inhomogeneous air flow can induce air density variations and thus refractive index variations along the light path of the trapping laser, which could cause power

fluctuations at the focus spot. Clear vinyl sheets were used to create an isolated environment around the setup, which prevents turbulent air currents generated from the air conditioner or people's movements affecting the trapping beam. This greatly improves the stability of the optical trap.

Software

Most of the control software of the microscope was developed in Igor Pro (Igor Pro 6, WaveMetrics, USA). The Igor NIDAQ package provides drivers for data acquisition board and GPIB interface, which allows direct access to these components from Igor. A full package of Igor procedures was developed for piezostage control, data acquisition of the signal from QPD, online alignments of the QPD and offline calibrations of the optical trap.

Detailed accounts of the three-dimensional detection of the trapped particle with QPD is discussed in the next section.

2.3.2 Forward-scattered light interferometry and calibration of PFM

Forward-scattered light interferometry for three-dimensional position detection

The method of detecting three-dimensional position of the trapped particle using laser interferometry was developed by Pralle *et. al.* [35]. As illustrated in Figure 2.3 A, a QPD is placed at the back focal plane of the condenser receiving the forward scattered light from the particle and unscattered light of the trapping laser. Naturally, the lateral displacement of the trapped particle away from the optical axis will result in changes in intensity distributions on four quadrants. Thus, the lateral displacements are proportional to the differential signals between two halves as

$S_x = (Q_1 + Q_2) - (Q_3 + Q_4)$ and $S_y = (Q_1 + Q_3) - (Q_2 + Q_4)$. Along the axial direction, the wave front of the Gaussian laser beam experiences a phase shift from $-\frac{\pi}{2}$ to $\frac{\pi}{2}$ with respect to the plane wave when it passes the focus [63]. Depending on the axial position of the trapped particle, the forward scattered light will have a phase difference relative to the unscattered light. When the scattered light and unscattered light interfere, the total intensity would be modulated by the particle's axial displacements. Thus the axial displacement of the particle is proportional to the total light intensity received at all four quadrants as $S_z = Q_1 + Q_2 + Q_3 + Q_4$. This detection method can easily achieve nanometer resolution in all three dimensions.

As shown in Figure 2.2, the QPD is an InGaAs PIN diode (G6849, Hamamatsu Photonics, Japan) with 2.0 mm in diameter and a dead zone of 0.1 mm in width between the quadrants. The photosensitivity is 0.67 A/W at 1064 nm. Signals generated from each quadrant of QPD are first amplified by the preamplifier with a gain of 20 V/mA (Offner MSR-Technik, Germany). After the preamp, signals are conditioned by a differential amplifier with variable gains (Offner MSR-Technik, Germany) to generate the corresponding S_x, S_y and S_z signals. This differential amplifier has a cut-off frequency of 800 KHz. A data acquisition board (NI-6120, National Instrument, USA) with 16 bits resolution and a maximum sampling rate of 1 MS/s for all 4 channels is used to digitize the signals from the differential amplifier and transfer them to the control computer.

The response of the detector was measured by scanning an immobilized 1 μm polystyrene sphere across the focus in three dimensions. Data along x and z is shown in Figure 2.3 B. For small displacements from the focal center, the detector response is linearly proportional to the displacements. However, when the particle's displacement is large (> 200 nm for x and > 400 nm for z), significant nonlinearity

of the detector response occurs.

Calibration of optical trap

Raw position signals recorded with the quadrant photodiode detector are in units of volts, which have to be converted into units of meters. To do this, three calibration factors along x, y and z need to be attained. The following calibration method can be applied: First, the position autocorrelation function is fitted with an exponential function as Equation (2.7) to get the position autocorrelation time τ.

$$f(t) = A_0 + A_1 exp(-\frac{t}{\tau}) \tag{2.7}$$

where τ is given by $\tau = \gamma/k$ assuming a Brownian particle in a harmonic potential [64], where $\gamma = 6\pi\eta r$ is the Stokes' drag coefficient for a sphere with radius r in a fluid with viscosity η and k is the stiffness of the trap. With a known r and η, the stiffness k can be readily calculated from τ. Figure 2.4 B shows the exponential fit to the position autocorrelation function along the y axis of a 200 nm polystyrene particle trapped with a laser power of about 26 mW at the focus spot. Second, a histogram of position signals is fitted with a Gaussian function (Equation (2.8)) as shown in Figure 2.4 C, which gives the width of the distribution σ_{volt}.

$$f(x) = B_0 + B_1 exp(-\frac{(x - B_2)^2}{2\sigma^2}) \tag{2.8}$$

Using the equipartition theorem, the width of distribution is related to thermal energy as $kS^2\sigma_{volt}^2 = k_B T$, where S is the calibration factor with a unit of V/m, k_B is the Boltzmann constant and T is the temperature [53]. Using this method, we obtained calibration factors for this experiment $S_x = 3.38 \times 10^7$ V/m, $Sy =$

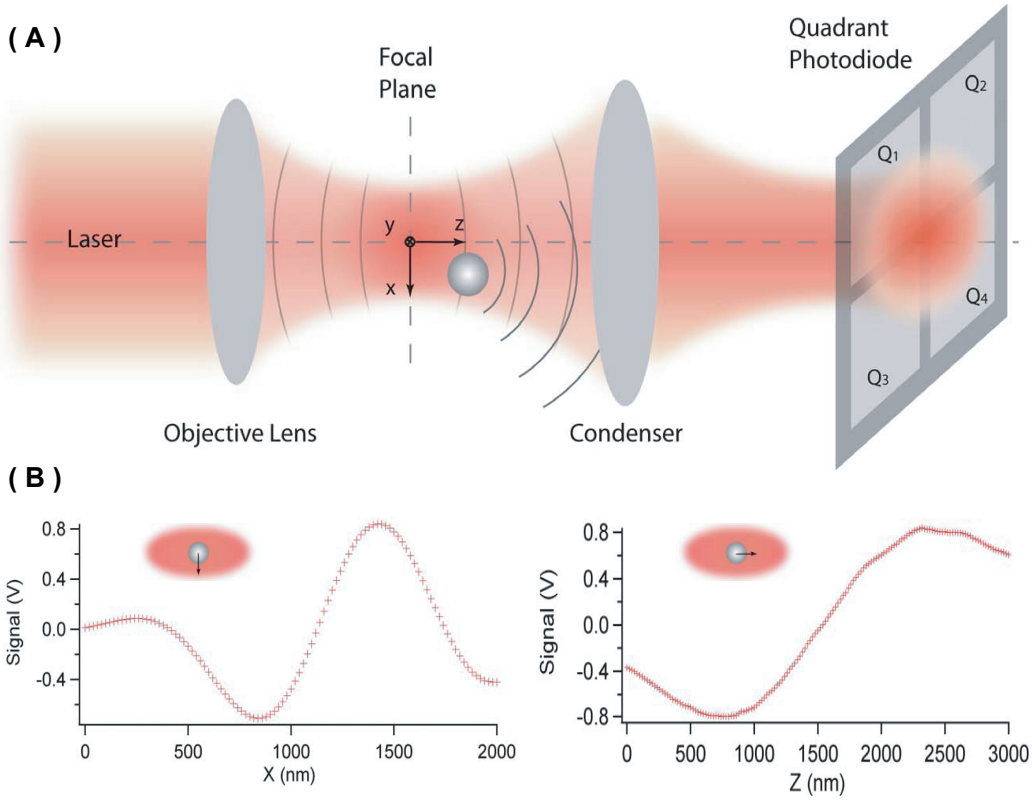

Figure 2.3: Three-dimension position detection of the trapped particle with a quadrant photodiode. (A) shows a quadrant photodiode placed at back focal plane of condenser receiving the interference intensity of forward-scattered light from the trapped particle and unscattered laser light. (B) shows the detector responses when an immobilized 1 μm polystyrene particle scans across the focus spot laterally along x and axially along z. Linear response regions of the detector are seen both on x and z.

2.82×10^7 V/m, and $S_z = 1.00 \times 10^7$ V/m from the raw position data.

The energy profile of the optical trap can be obtained from the position histogram (or position probability distribution) using Boltzmann statistics [53]. The position probability distribution is given as:

$$p(x) = Ce^{-\frac{E(x)}{k_B T}} \tag{2.9}$$

Thus the energy profile can be solved as:

$$\frac{E(x)}{k_B T} = -lnp(x) + lnC \tag{2.10}$$

The trapping potential obtained from Figure 2.4 (C) is shown in (D). We can see that the potential is very close to a harmonic that can be well fitted with a second order polynomial.

Correction of detector nonlinearity

When the particle' excursion is large, e.g. > 100 nm, the nonlinearity of the detector (smaller detector sensitivity for larger displacement) may introduce some artifacts in the position signal that have to be corrected. This is especially true for thermal noise imaging in which less laser power is used for larger excursion of the particle. The nonlinearity of the detector can be corrected on each axis in all three dimensions by assuming a constant diffusion coefficient of the particle independent of the particle's position in the optical trap [66]. This is valid when the particle is far from any objects. When the particle is close to some surfaces, the hydrodynamic interactions as a result of non-slip boundary conditions would introduce a distance-dependent viscous coefficient and thus the distance-dependent diffusion constant [67, 68]. So

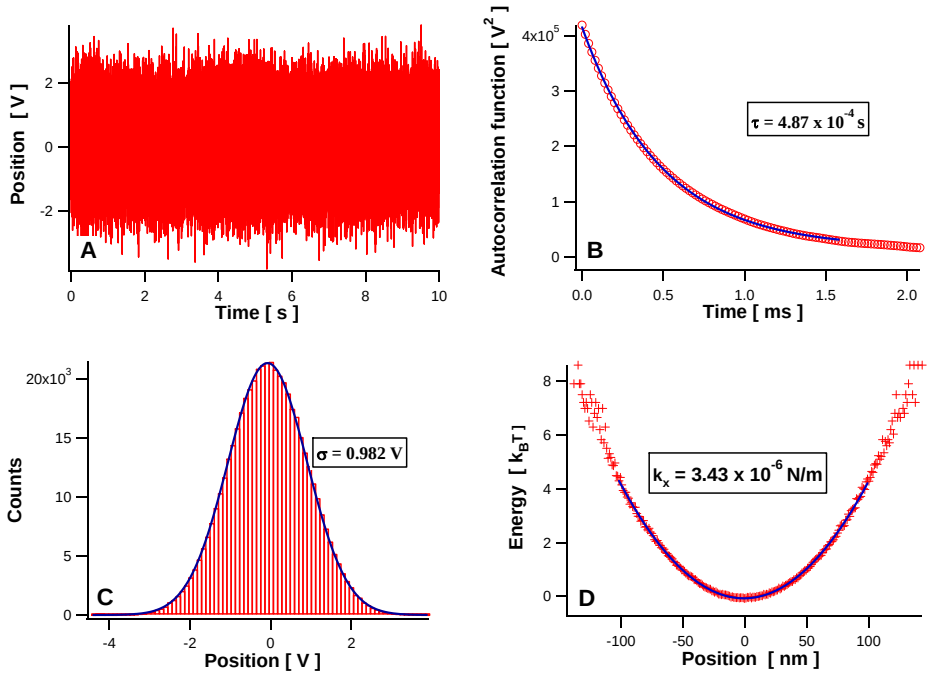

Figure 2.4: Calibration of position data in the photonic force microscope. The position autocorrelation function (B) and the position histogram (C) of the raw position signals (A) and the energy profile (D) of the trap along the y-axis are shown respectively. The trapped particle was a 200 nm polystyrene sphere and the laser power at the focus spot was about 26 mW. The signals were sampled at 50 KHz for 10 seconds in all three dimensions simultaneously. The autocorrelation function (red circles in B) was fitted with an exponential function (blue curve in B), which gave a position autocorrelation time of $\tau = 0.487$ ms. A Gaussian function (blue curve in C) fitted to the position histogram (red bars in C) gave the width of the distribution as $\sigma = 0.982$ V. (D) shows the energy profile of the trap (red +) obtained from the position histogram by Boltzmann statistics. A second order polynomial fit (blue curve) gave the stiffness of the trap as 3.43×10^{-6} N/m, which is in good agreement with the stiffness obtained in (B).

if the diffusion coefficient can be assumed to be constant over the entire trapping volume, the local detector sensitivity can then be acquired from the the local variance as follows:

$$var(\Delta V)|_{V_0} = (\partial_x \Delta V|_{V_0})^2 var(\Delta x) = (\partial_x \Delta V|_{V_0})^2 2Dt \tag{2.11}$$

where the variance is only evaluated for the position data falling into $[V_0 - \Delta V, V_0 + \Delta V]$, $D = k_B T/6\pi\eta r$ is the diffusion constant and $\partial_x \Delta V|_{V_0}$ is the local detector sensitivity (or the local slope of the detector response as shown in Figure 2.3 B) at V_0. Thus the local detector sensitivity can be obtained from Equation (2.11) as:

$$\partial_x \Delta V|_{V_0} = \sqrt{\frac{var(\Delta V)|_{V_0}}{2Dt}} \tag{2.12}$$

Knowing all the local sensitivities, the position signals in meters can be obtained by integrating from a reference point as follows:

$$x(V) = \int_{V_{min}}^{V} \frac{1}{\partial_x \Delta V|_{V'}} dV' + x_{ref} \tag{2.13}$$

The detector sensitivity and the position histogram in all three dimensions of a 200 nm polystyrene particle before and after correction for nonlinearity are shown in Figure 2.5. We can see that the position signal along the optical axis z is shows larger nonlinearity than its lateral components. This can be explained by the fact that the equilibrium position along the optical axis is not at the geometrical focus plane, but rather at a position displaced away from the focus plane along the direction of light propagation. This brings the particle to the detector's nonlinear region so that we see a strong nonlinear effect along z. Nonlinear effects along lateral dimensions are small when the particle's excursion is below 100 nm. Figure 2.5 B shows the detector sensitivity and the position histogram after the correction of

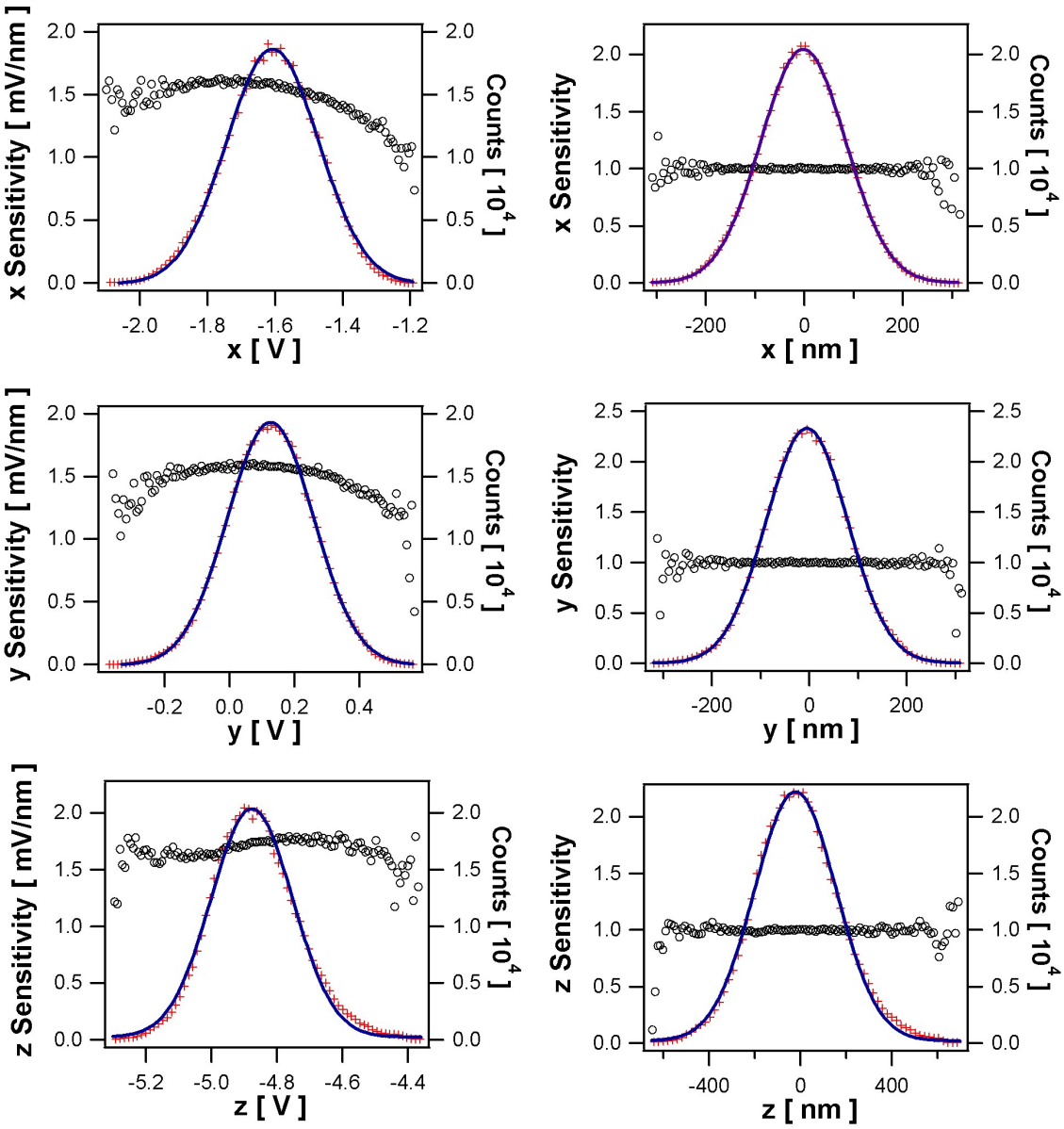

Figure 2.5: Detector sensitivity and position histogram for both raw signal (A) and signal after correction for nonlinearity (B). Significant nonlinear detector response presents for larger excursions. The sensitivities calculated from corrected position signals show constants values. Experimental data were sampled at 50 KHz for 5 seconds for a 200 nm polystyrene particle in the optical trap.

nonlinearity . In this situation we see a constant detector sensitivity along each dimension and a more symmetric trapping volume.

Note that here we have assumed that the detector nonlinearity along one axis depends only on the particle's position at that dimension. In reality, the detector sensitivity is actually a function of both x, y and z. In this case, it is much more complicated to correct for the nonlinearity contained in the signal. One of the ways to do this is to measure the detector response on a bead immobilized by polymer gels in three dimensions while scanning it across the focus spot in three dimensions and acquire the sensitivity at each position in the trapping volume. However, such a method cannot fully reproduce the experimental conditions and other errors are introduced such as errors caused by the refractive index difference between the polymer gels and the medium used in the experiment.

Long-term stability of PFM

The long term stability of PFM is acquired by measuring the positions of an immobilized 1 μm polystyrene particle located at the focal center with QPD over a time period of 150 seconds. The data is shown in Figure 2.6. Along the lateral dimensions, the drift is very small with a maximum amplitude less than 8 nm. The drift along the optical axis is larger but still within reasonable ranges with an average of about 0.3 nm/s. Note that the position fluctuations of the fixed particle are disturbed by a sum of different noise sources, including laser power fluctuations and pointing instability, drift of mechanical parts etc. The objective lens used here is a water immersion lens so that the long term drift induced by the evaporation of immersion fluid is expected to be larger than the typical oil immersion lens.

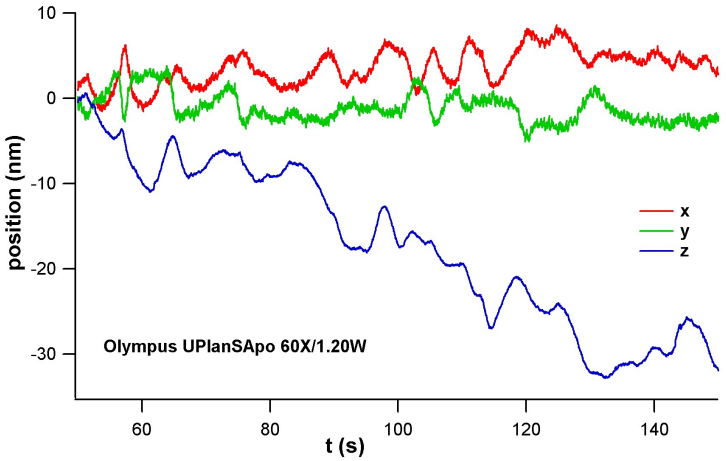

Figure 2.6: Long-term stability of the photonic force microscope. Position signals from QPD for a 1 μm polystyrene particle immobilized on a coverslip were sampled at 1 KHz for 150 seconds. The data was smoothed with a box size of 100 points.

2.3.3 Summary

A photonic force microscope was developed with the capability to trap microscopic particles and follow its Brownian motion in three dimensions with nanometer resolution and about 1 MHz bandwidth. Fluorescence microscopy and bright field imaging were incorporated into the microscope for visualizing the trapped particle. Special care was taken to maintain the long term stability of the setup. Calibrations and correction for nonlinearity of position data allows the Brownian motion of the particle to be correctly followed, which permits the application of the photonic force microscope to thermal noise imaging etc.

Chapter 3

Brownian motion at fast time scales

This chapter first reviews theories of Brownian motion at fast time scales under the particle's inertia effect and the hydrodynamic memory effect. Previous experimental studies of inertia effects in Brownian motion and our motivations for observing Brownian motion in faster time scales are also described. Special requirements of the instruments for observing Brownian motion are discussed and incorporated into conventional PFM. The hydrodynamic memory effect of the fluid and the particle's inertia effect are clearly shown with our experimental data. The excellent agreement between our data and the Hinch theory [81] indicates that the continuum hydrodynamic theories of Brownian motion is valid down to the ballistic regime.

3.1 Historical reviews and motivations

As a fundamental phenomenon in nature, Brownian motion has profound impacts on many different disciplines including physics, chemistry, biology, and even math-

ematics and finance [69, 70]. Brownian motion was named after renowned British botanist Robert Brown after he discovered the erratic motions of microscopic particles suspended in fluid in 1827 [71]. Although these types of random motions were observed earlier by others, Brown was the first one who did systematic studies and many control experiments to conclude that such motions are due to neither the living origin of the moving particles nor the evaporation of the ambient fluid. The origin of Brownian motion remained an intriguing subject for theoretical speculation as well as experimental investigation until the beginning of the 20^{th} century. There were several notable attempts during this period [69]. In 1863, Christian Wiener suggested that the random motions of suspended particles must be due to internal molecular motions in the fluid. From today's viewpoint, Wiener's suggestion is practically correct, however it was based on the concept of aether atom which was popular in his day. From 1874 to 1880, the idea of molecular fluctuations as the root of Brownian motion was suggested by J. Delsaux, J. Thirion and X. Carbonelle though they did not derive any quantitative results. It is interesting to note that most modern mathematical ideas about Brownian motion were developed by mathematician Louis Bachelier in 1990 in a study of stochastic process in the stock market.

In his 1905 paper, Einstein successfully explained the random motion as the amplification of the statistical fluctuations of the surrounding fluid molecules [72]. As a consequence of this random motion, the average position fluctuation remains zero while the mean square displacement (MSD) that accounts for the average distance explored by the particle evolves as $2Dt$, where D is the diffusion constant and t is the elapsed time. Einstein's theoretical predictions were later verified by J. Perrin in his experiments in 1908 [73, 74]. The diffusion constant D can be related

to the Stokes' drag coefficient γ by thermal energy as $D = k_B T/\gamma$. This so-called Stokes-Einstein relationship is one of examples of the fluctuation-dissipation theorem, which indicates that the fluctuation of the particle at rest has the same origin as the dissipative frictional force one must experience if trying to perturb the system in a particular direction. This fluctuation-dissipation relationship has essential influences on other subjects in physics, and has become the theoretical background for experiments such as microrheology [75] that uses Brownian motion to probe the properties of the environment . Another account of Brownian motion based on molecular-kinetic theory was developed by Smoluchowski at around the same time as Einstein. His results predicted the same evolution of MSD over time with a minor error in the coefficient [76].

Einstein did note that his statistical approach will break down as time approaches zero, wherein the inertia effect of the particle becomes dominant and the motion becomes correlated. The first mathematical description of a particle's dynamics over the entire time domain was provided by Langevin [77]. The particle's inertia results in an exponentially decayed velocity autocorrelation function with a characteristic time scale $\tau_p = m/\gamma$, where m is the mass of a spherical particle. For a 1 micrometer silica particle, τ_p is on the order of 10 ns. The MSD is proportional to t^2 around τ_p and recovers Einstein's result $2Dt$ at long time scales. This t^2 dependent MSD is conventionally referred as the ballistic regime since the particle seems to move with a constant velocity at this time scale.

Langevin took Stokes' law $f = -\gamma\dot{x}$ to describe the frictional forces experienced by the Brownian particle. However, Stokes' friction law is only valid for slow steady motions in viscous flow and can not correctly describe the case in Brownian motion. The major discrepancy is due to the nonnegligible fluid inertia effect. When

the suspended particle moves, it has to drag and displace its surrounding fluid. The surrounding fluid will develop flow patterns which can influence the particle's dynamics at a later time – the so-called hydrodynamic memory effect. These coherent flow patterns have been demonstrated by Alder and Wainwright in molecular dynamic simulations of fluid molecules [78, 79]. The fluid inertia introduces a new characteristic time scale $\tau_f = \rho_f r^2/\eta$, which is the time it takes for the vortices to diffuse a distance of one particle radius r in a fluid of density ρ and viscosity η. τ_f is about 0.25 μs for 1 micrometer particle. Theories considering the fluid inertia effect on Brownian motion were first developed in 1945 [80], and later brought to wider attention by Hinch in 1975 [81]. The details of the theories of Brownian motion will be reviewed in the next sections.

3.1.1 Theory of Brownian motion at fast time scales

Navier-Stokes equation for incompressible fluid

For most fluids, when the time scale considered is significantly larger than the time scale of sound propagation τ_c [1], the fluid can be considered incompressible, e.g. the density of fluid is spatially invariant. In this case, the fluid surrounding a Brownian particle can be described by the Navier-Stokes equation for an incompressible fluid as Equation (3.1), where $\vec{v}$ is the flow velocity, ρ_f is the fluid density, p is the pressure, $\mathbb{T}$ is the stress tensor and $\vec{f}$ represents body forces such as gravity or centrifugal force [82].

$$\rho_f \frac{\partial \vec{v}}{\partial t} + \rho_f(\vec{v}\cdot\nabla)\vec{v} = -\nabla p + \nabla\cdot\mathbb{T} + \rho_f\vec{f} \tag{3.1}$$

[1] This time scale is defined as the time required for a sound wave to traverse a sphere radius: $\tau_c = r/c_{sound}$. For a particle with radius $r = 1$ μm in water ($c_{sound} \approx 1500$ m/s), τ_c is about 1 ns.

The first term $\rho_f \frac{\partial \vec{v}}{\partial t}$ describes the acceleration due to the time-dependent velocity variation. The nonlinear term $\rho_f(\vec{v}\cdot\nabla)\vec{v}$ gives the convective acceleration: the effect of time independent acceleration of a fluid with respect to space. In a Newtonian fluid where the stress is linearly proportional to the rate of strain, the stress term $\mathbb{T}$ simplifies to $\eta\nabla^2\vec{v}$, where η is the viscosity of the fluid. It gives the friction force coming from the viscous fluid.

The importance of those two inertial terms at the left hand side of Equation (3.1) can be characterized by two dimensionless numbers [83]. The first one is Reynolds number, which gives a measure of the ratio of inertia force $\rho_f(\vec{v}\cdot\nabla)\vec{v}$ to viscous forces $\eta\nabla^2\vec{v}$ as defined in Equation (3.2), where v is the velocity and d is the characteristic dimension of the fluid flow.

$$Re = \frac{\rho_f v d}{\eta} \tag{3.2}$$

For low Reynolds number flow, which is the case for a Brownian particle moving within a resting fluid, the inertial term due to convective effects can be neglected and thus the Navier-Stokes equation can be linearized. This generally simplifies the problem significantly.

The second parameter is defined as the ratio of term $\rho_f \frac{\partial \vec{v}}{\partial t}$ to the viscous term $\eta\nabla^2\vec{v}$, which is given by Equation (3.3), where τ is the typical time scale associated with the flow [83].

$$N = \frac{\rho_f d^2}{\eta\tau} \tag{3.3}$$

When $N \ll 1$, the response of the fluid to external forces can be considered instantaneous; while in the range of $N \geq 1$, the inertia of the fluid plays an important role in the dynamics. So for low Reynolds number flow, the inertial effect of the fluid

can still be significant if N is not small.

Langevin equation and the inertia effects of the Brownian particle

The equation of motion for a Brownian particle moving in a fluid is given by the Langevin equation as shown in Equation (3.4), where F_{fr} is the friction force, F_{th} is the randomly fluctuating thermal forces and F_{ext} is any possible external forces. The sum of F_{fr} and F_{th} is the total force acting on the particle by its surrounding fluid.

$$m\ddot{x} = F_{fr} + F_{th} + F_{ext} \tag{3.4}$$

The perpetual erratic motions of the Brownian particles is a result of fluctuations in the collisions with its surrounding fluid molecules under thermal equilibrium. The suspending fluid can be treated as a hydrodynamic continuum whenever the size of the colloidal particles far exceeds that of the fluid molecules, and the number of collisions per unit of time is large. For typical colloidal particles, the ratio of the size of the particle to that of fluid molecules is typically around 10^4 (given that the radius of the particle is 1 μm and the size of water molecule is about 1 Å). Under normal conditions, the number of collisions in a second that a Brownian particle experiences is on the order of 10^{20}, under which separate collisions are usually not considered [2]. So the separation of forces acting by the fluid into F_{fr} and F_{th} is readily justified in the Langevin equation. F_{fr} represents a systematic friction force experienced by the particle and F_{th} represents the random fluctuations in addition to the friction force. F_{th} is assumed to be independent of velocity $\dot{x}$ and varies extremely rapidly compared to the variations of velocity $\dot{x}$ [84]. Its magnitude can

[2]The number of collision per second can be estimated from the equation $n = \frac{\pi r^2 v_f \rho_f}{M_f}$, where r is the radius of the Brownian particle, $v_f = \frac{k_B T}{M_f}$ is the mean velocity of fluid molecules and M_f is the mass of an individual fluid molecule.

be related to thermal energy k_BT as Equation (3.5).

$$\langle F_{th}(t)F_{th}(t')\rangle = 2\gamma k_B T\delta(t-t') \tag{3.5}$$

In the Stokes' friction limit where $Re \ll 1$ and $N \ll 1$, the friction force is instantaneously proportional to the velocity of the particle as in Equation (3.6), where γ is the Stokes's drag coefficient with $\gamma = 6\pi\eta r$ for a sphere with radius r.

$$F_{fr} = -\gamma\dot{x} \tag{3.6}$$

For a free particle in which $F_{ext} = 0$, the Langevin equation can be solved giving the velocity autocorrelation function as indicated in Equation (3.7), which decays exponentially with a characteristic time scale of $\tau_p = m/\gamma$. τ_p indicates the time scale in which the inertia of the particle dominates the motion. The successive motions of the Brownian particle is strongly correlated within this time scale. Correlation lasts longer for more massive particles and smaller viscous drag coefficients.

$$C(t) = \langle v(t)v(0)\rangle = \frac{k_BT}{m}e^{-t/\tau_p} \tag{3.7}$$

When $t = 0$, $C(0) = v^2 = \frac{k_BT}{m}$, which fulfills the equipartition theorem for a Brownian particle.

The mean square displacement can be obtained by integrating the velocity autocorrelation function using the following relation:

$$\langle[\Delta x(t)]^2\rangle = 2\int_0^t (t-t')C(t')\,dt' \tag{3.8}$$

The result is shown as:

$$\langle[\Delta x(t)]^2\rangle = 2Dt[1 + \frac{\tau_p}{t}(e^{-t/\tau_p} - 1)] \tag{3.9}$$

where $D = k_B T/\gamma$ is the diffusion constant of the particle.

For $t \to \infty$, the mean square displacement approaches its value at the diffusive regime indicating that the particle is undergoing random motions.

$$\langle[\Delta x(t)]^2\rangle = 2Dt \quad \text{for} \quad t \to \infty \tag{3.10}$$

For $t \to 0$, the motion of the particle approaches the ballistic regime where the mean square displacement is given as:

$$\langle[\Delta x(t)]^2\rangle = \frac{k_B T}{m} t^2 \quad \text{for} \quad t \to 0 \tag{3.11}$$

The mean square displacement scales with t^2, indicating that the particle is moving with a constant velocity of $\sqrt{\frac{k_B T}{m}}$. At the time scale of $0.1\tau_p$, the mean square displacement already reaches about 90% of its ballistic value, indicating that the particle is close to ballistic motion. However, at this time scale the particle still has a large amount of collisions with its surrounding fluid molecules. The average number of collisions would be around 10^{11} for a polystyrene particle of density 1.06 g/cm^3 and 1 μm diameter with $\tau_p = 0.06$ μs. If a water molecule with weight M_w traveling with speed $c = \sqrt{k_B T/M_w} = 370$ m/s collides with the polystyrene particle, the latter would recoil and pick up a speed of 2×10^{-6} cm/s in a single collision, which is about 7×10^{-6} times the speed of the particle at the ballistic regime. In this case, the center of gravity of the particle might take a complicated zigzag path, but the magnitude of displacement is so small that the average path might still remain

smooth in the observable limit. So in this time scale, we should still view Brownian motion as a macroscopic phenomenon rather than motion composed of discrete collisions. We can think of it as caused by fluctuations in the bulk properties of the fluid in the neighborhood of the particle, more specifically of pressure fluctuations due to statistical fluctuations in the number of molecules in a volume of an order of magnitude of the volume of the Brownian particle.

Stokes-Boussinesq friction and the hydrodynamic memory effect

In Stokes flow, the long-range propagation of stress within the fluid is instantaneous. However, over a short time interval, the inertia of the fluid should confine any instantaneous disturbance to a small region [83]. This is the case in the Stokes-Boussinesq limit where the acceleration due to time-dependent velocity variation is no longer negligible, e.g. $N \geq 1$. The Stokes-Boussinesq friction force takes the form as indicated by Equation (3.12). This friction force can be derived by solving the time-dependent linearized Navier-Stokes equations [85, 86].

$$F_{fr} = -\gamma \dot{x}(t) - \frac{1}{2} m_0 \ddot{x}(t) - 6r^2 \sqrt{\pi \rho \eta} \int_0^t \frac{1}{\sqrt{t-\tau}} \ddot{x}(\tau)\, d\tau \tag{3.12}$$

The first term on the right hand side of Equation (3.12) is the normal Stokes friction force, and the second term is associated with the inertia of the co-moving fluid where $m_0 = \frac{4}{3}\pi r^3 \rho_f$. The third term describes the hydrodynamic memory effect associated with the particle's acceleration history in the viscous unsteady flow.

The characteristic time scale of the hydrodynamic memory effect is given when $N \sim 1$, which is

$$\tau_f = \frac{\rho_f r^2}{\eta} \tag{3.13}$$

The physical meaning of this characteristic time scale is the time it takes for a vortex to diffuse at a distance of one particle radius.

In the Stokes-Boussinesq regime, the Langevin equation for a free particle ($F_{ext} = 0$) can be written as

$$m^* \ddot{x} = -\gamma \dot{x} - 6r^2\sqrt{\pi\rho\eta} \int_0^t \frac{1}{\sqrt{t-\tau}} \ddot{x}(\tau)\, d\tau + F_{th} \tag{3.14}$$

where $m^* = m + \frac{1}{2}m_0$ is the effective mass of the particle. Solving the above Langevin equation gives the velocity autocorrelation function as

$$C(t) = \frac{k_B T}{m^*(\alpha_+ - \alpha_-)}[\alpha_+ exp({\alpha_+}^2 t) erfc(\alpha_+\sqrt{t}) - \alpha_- exp({\alpha_-}^2 t) erfc(\alpha_-\sqrt{t})] \tag{3.15}$$

where

$$\alpha_\pm = \frac{3}{2}[\frac{3 \pm (5 - 36\tau_p/\tau_f)^{1/2}}{\sqrt{\tau_f}(1 + 9\tau_p/\tau_f)}] \tag{3.16}$$

As $t \to 0$, the velocity autocorrelation function approaches

$$\lim_{t\to 0} C(t) = \frac{k_B T}{m^*} \tag{3.17}$$

Note here that the mean speed of the particle is given by $\sqrt{k_B T/m^*}$, which is in contradiction with the equipartition theorem for the Brownian particle because the effective mass of the particle m^* is greater than the mass of the particle m. This paradox was resolved by Zwanzig and Bixon in 1975 [87]. If considering a fluid with a very small compressibility, the velocity autocorrelation function of the particle has a rapid decay from $k_B T/m$ to $k_B T/m^*$ at the time scale of sound propagation in a fluid τ_c. This initial decay is due to acoustic damping of the particle velocity, and occurs even when the fluid is inviscid. If the fluid is inviscid, the velocity autocorrelation

function will remain as k_BT/m^* after the initial decay. When the fluid is viscous, the velocity autocorrelation function has a slower decay from k_BT/m^* to zero after the initial decay just as if the fluid were incompressible as the case being considered here.

The long-time behavior of the velocity autocorrelation function can be attained using the asymptotic expansion of the product of the exponential function and complex error function, which is

$$C(t) \simeq \frac{k_BT\rho^{1/2}}{12(\pi\eta)^{3/2}} t^{-\frac{3}{2}} \quad \text{for} \quad |\alpha_{\pm}^2|t \gg 1 \tag{3.18}$$

The power law decay of the velocity autocorrelation function is drastically different from the exponential decay in the Stokes limit case, which is normally referred to as long time tail. This prolonged correlation is due to the propagation of flow patterns within the fluid, which can act back on the particle at a later time. Thus, the fluid seems to have memory that can preserve the information of the particle's past motion.

The mean square displacement of the particle under Stokes-Boussinesq friction is given as follows

$$\langle[\Delta x(t)]^2\rangle = 2Dt[1 - 2\sqrt{\frac{1}{\pi}\frac{\tau_f}{t}} + \frac{8}{9}\frac{\tau_f}{t} - \frac{\tau_p}{t} + \Omega(\frac{\tau_p}{\tau_f}, \frac{t}{\tau_f})] \tag{3.19}$$

where

$$\Omega(\frac{\tau_p}{\tau_f}, \frac{t}{\tau_f}) = \frac{3}{t(5\tau_f - 36\tau_p)^{1/2}} \times (\frac{1}{\alpha_+^3} e^{\alpha_+^2 t} erfc(\alpha_+\sqrt{t}) - \frac{1}{\alpha_-^3} e^{\alpha_-^2 t} erfc(\alpha_-\sqrt{t}))] \tag{3.20}$$

The asymptotic behavior of the mean square displacement is given by the following

$$\lim_{t\to\infty}\langle[\Delta x(t)]^2\rangle = 2Dt$$

$$\lim_{t\to 0}\langle[\Delta x(t)]^2\rangle = \frac{k_B T}{m^*}t^2$$

The mean square displacement again approaches the diffusive regime in the long time scale. At the short time scale when $t \to 0$, the motion again approaches the ballistic regime however with the mass substituted with the effective mass of the particle m^*. In the time scale between these two limits, the motion of the particle is dominated by the hydrodynamics memory effect and is rather complex.

Brownian motion within an optical trap

When the displacement of the trapped particle away from the trapping center is small (usually below 100 nm), the external force resulting from the radiation pressure is linearly proportional to the displacement [33, 36, 65]. Thus the particle experiences thermal motions within an harmonic potential with F_{ext} given by

$$F_{ext} = -kx \tag{3.21}$$

where k is the spring constant of the harmonic potential.

Under the Stokes friction limit, the equation of motion is given as

$$m\ddot{x} = -\gamma\dot{x} + F_{th} - kx \tag{3.22}$$

The velocity autocorrelation function is then solved as

$$C(t) = \frac{k_B T}{m(\beta_+ - \beta_-)}[\beta_+ e^{-\beta_+ t} - \beta_- e^{-\beta_- t}] \tag{3.23}$$

where

$$\beta_\pm = \frac{1}{2\tau_p}(1 \pm \sqrt{1 - 4\tau_p/\tau_k})$$

and τ_k is the autocorrelation time of the harmonic potential given by $\tau_k = \gamma/k$.

The asymptotic behavior of the velocity autocorrelation function at the time scales around τ_p and τ_k is given by the following:

$$C(t) \propto e^{-t/\tau_p} \quad \text{for} \quad t \approx \tau_p$$

and

$$C(t) \propto -e^{-t/\tau_k} \quad \text{for} \quad t \approx \tau_k$$

Note that the asymptotic behavior around τ_p is the same as in the case of the free particle where $F_{ext} = 0$, indicating the particle's motion at the short times is not affected by the confinement of the optical trap. This is normally the case since τ_p is usually 2 or more orders of magnitude smaller than τ_k for the typical optical traps, which also justifies the use of optical trap to study Brownian motion at fast time scales. Another interesting feature is that the velocity autocorrelation function becomes negative at time scales around τ_k. This is due to the nature of the restoring force in an harmonic potential. Whenever the particle fluctuates away from the potential minimum, the restoring force tends to pull it back to the potential minimum position and thus constantly changes the direction of the velocity.

The mean square displacement in this case is given as

$$\langle[\Delta x(t)]^2\rangle = \frac{2k_BT}{k}[1 + \frac{\beta_-}{\beta_+ - \beta_-}e^{-\beta_+ t} + \frac{\beta_+}{\beta_- - \beta_+}e^{-\beta_- t}] \tag{3.24}$$

with its asymptotic value approaching

$$\langle[\Delta x(t)]^2\rangle = \frac{2k_BT}{k} \quad \text{for} \quad t \to \infty$$

The constant value at the long time limit is set by thermal energy, indicating that the particle is exploring the energy landscape of the harmonic potential under thermal agitation.

Under the Stokes-Boussinesq friction, the Langevin equation for an optically trapped particle is given by Clercx *et al.* [88]

$$m^*\ddot{x} = -\gamma\dot{x} - 6r^2\sqrt{\pi\rho\eta}\int_0^t \frac{1}{\sqrt{t-\tau}}\ddot{x}(\tau)\,d\tau + F_{th} - kx \tag{3.25}$$

Solving this equation of motion gives the velocity autocorrelation function as follows

$$\begin{aligned} C(t) =& \frac{k_BT}{m^*}[\frac{z_1^3 e^{(z_1^2 t)} erfc(z_1\sqrt{t})}{(z_1-z_2)(z_1-z_3)(z_1-z_4)} + \frac{z_2^3 e^{(z_2^2 t)} erfc(z_2\sqrt{t})}{(z_2-z_1)(z_2-z_3)(z_2-z_4)} \\ &+ \frac{z_3^3 e^{(z_3^2 t)} erfc(z_3\sqrt{t})}{(z_3-z_1)(z_3-z_2)(z_3-z_4)} + \frac{z_4^3 e^{(z_4^2 t)} erfc(z_4\sqrt{t})}{(z_4-z_1)(z_4-z_2)(z_4-z_3)}] \end{aligned} \tag{3.26}$$

where z_1, z_2, z_3 and z_4 are the four roots of the equation

$$(\tau_p + \frac{1}{9}\tau_f)x^4 - \sqrt{\tau_f}x^3 + x^2 + 1/\tau_k = 0$$

The asymptotic behavior at $t \simeq \tau_f$ of the velocity autocorrelation function

is given by the following

$$C(t) \simeq \frac{45k_BTr^2}{4k^2}\sqrt{\frac{\rho_f\eta}{\pi}}t^{-7/2} \quad \text{for} \quad |z_i^2|t \gg 1 \quad \text{where} \quad i = 1,2,3,4 \tag{3.27}$$

Again we obtain a long time tail with an exponent of $-\frac{7}{2}$, which is different from the free particle case where $C(t) \propto t^{-3/2}$.

The short time limit is given as

$$\lim_{t\to 0} C(t) = \frac{k_BT}{m^*} \tag{3.28}$$

which again approaches the same value as in the free particle case.

The mean square displacement in this case is given as

$$\begin{aligned}\langle[\Delta x(t)]^2\rangle =& \frac{2k_BT}{k} + \frac{2D}{\tau_p + 1/9\tau_f}[1 + \frac{e^{z_1^2t}erfc(z_1\sqrt{t})}{z_1(z_1-z_2)(z_1-z_3)(z_1-z_4)} \\ & \frac{e^{z_2^2t}erfc(z_2\sqrt{t})}{z_2(z_2-z_1)(z_2-z_3)(z_2-z_4)} + \frac{e^{z_3^2t}erfc(z_3\sqrt{t})}{z_3(z_3-z_1)(z_3-z_2)(z_3-z_4)} \\ & \frac{e^{z_4^2t}erfc(z_4\sqrt{t})}{z_4(z_4-z_1)(z_4-z_2)(z_4-z_3)}]\end{aligned} \tag{3.29}$$

The long time limit of the mean square displacement is

$$\lim_{t\to\infty}\langle[\Delta x(t)]^2\rangle = \frac{2k_BT}{k} \tag{3.30}$$

which shows the confinement by the optical trap as $t \to \infty$.

When $t \ll \tau_k$, the effect of the harmonic potential is negligible. In this case the mean square displacement is given in Equation (3.19).

Summary

For a free particle, at the long time scale, all the inertia effects die out and the motion is random as predicted by previous theories. At the short time scale around τ_p, the motion is ballistic and dominated by the inertia of the particle and its surrounding fluid. Between these two regimes is the transition regime where motion is dominated by the hydrodynamic memory effect.

For a particle in an optical trap, at the time scale of $t \ll \tau_k$, the particle can be seen as a free particle moving in a viscous unsteady fluid without the effect of trapping forces. The effect of the harmonic potential changes the long time tail exponent from $-\frac{5}{2}$ to $-\frac{7}{2}$ at the time scale around τ_f, and results in a negative correlation at the time scale around τ_k. The confinement of the optical trap limits the mean square displacement to a constant value of $\frac{2k_BT}{k}$ as $t \to \infty$.

3.1.2 Previous studies of inertia effects in Brownian motion and our motivation

There have been several attempts to study the inertia effects on Brownian motion at fast time scales. One of them is to use diffusing wave spectroscopy (DWS) to study Brownian motions of colloidal suspensions at short time scales. In DWS, the information of many partciles' average motion can be obtained from the intensity autocorrelation of light scattered from the particles [89]. One of the important assumptions in DWS is that each photon has to be scattered a large number of times after the light passes through the sample, thus requiring a high concentration of particles in solution. In 1992, Zhu *et al.* showed the $t^{-3/2}$ decay of velocity correlations for 1.53 μm diameter polystyrene particles at a volume fraction of 2.1% [90]. In 1993, Kao *et al.* showed that the evolution of MSD agreed with Equation (3.19) for

0.205 μm polystyrene particles at a volume fraction of 2% [91]. The agreement with the theory was shown down to the time scales of $0.2\tau_f$, where $\tau_f = 12.5$ ns. They also found that the concentrated systems exhibited clear deviations from the isolated-particle theory described by Equation (3.19). This deviation can be explained by significant hydrodynamic interactions between adjacent particles mediated by sound waves when the concentration of the particles is high [92]. Thus the concentration of particles has to be kept very low to avoid this hydrodynamic interactions.

Brownian motion at fast time scales on single particles has been observed with photonic force microscopy recently [93]. The agreement with Equation (3.19) has been shown down to the time scale τ_f and the dominance of the hydrodynamic memory effect over the particle's inertia has been shown. However, Brownian motion of a single particle in the ballistic regime where the motion is dominated by the inertia of the particle has never been observed and thus theories for this regime have never been tested.

The main difficulty in the direct observation of ballistic motion is the coupling between the length scale and the time scale of Brownian motion. For example, a 1 μm Brownian particle will on average move about 1 nm within 1 μs. Resolving the Brownian motion at the ballistic regime requires an instrument with a combination of high temporal and spatial resolution. Although existing instruments can have feasible spatial resolution or temporal resolution, so far none of them have been able to meet both requirements at the same time.

3.2 Development of a fast position-sensitive detector

To observe Brownian motion at much faster time scales on single particles, the first step is to develop a fast position-sensitive detector for PFM that could surpass

the bandwidth and spatial resolution of the previous quadrant photodiode detector. Currently, the best quadrant photodiode detector system has 1 MHz bandwidth and 2×10^5 V/A of gain. As mentioned before, at faster time scales, the average amplitude of Brownian motion is also smaller. Thus, a detector with high gain (typically$\sim 10^5$) at high bandwidth is required to amplify the small intensity difference and resolve the position displacement of the trapped particle at this time scale.

There are several limiting factors in improving the bandwidth of the quadrant photodiode. First, the capacitance of the photodiode and the speed of the induced majority carriers can limit the response speed of the photodiode. This can be solved by reducing the area of the photodiode. For instance, a quadrant photodiode with radius of 1 mm (G6849-01, Hamamastu, Japan) can have 120 MHz cut-off frequency at 3 dB. However, an amplifier operating at such a bandwidth with reasonable gain has never been achieved for this QPD. Part of the reason is that the design of electronics is still an art. It is difficult to predict the performance of an amplifier from the first principle when the level of complexity increases. Second, the geometry and spatial arrangement of each quadrant in QPD could potentially increase the noise in position signals at high frequency. Four individual quadrants in QPD must be packed as close as possible to reduce the dead zone. This spatial arrangement increases the cross-talk between quadrants and eventually the noises in the signals at high frequency due to the interactions between induced high frequency currents in each quadrant. This is unavoidable since the closely-packed four quadrants has the function to spatially split the light beam into four parts for differential detection.

So the guiding philosophy in developing a faster detector is to separate the functions of a position sensitive detector so that each can be independently opti-

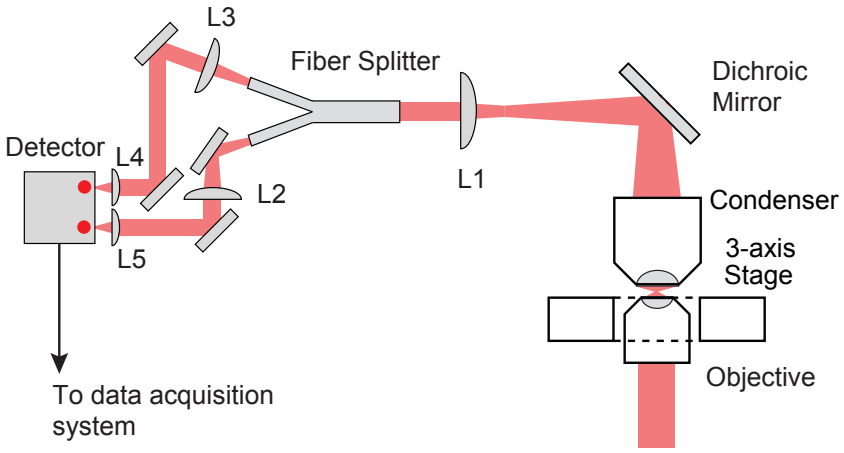

Figure 3.1: Photonic force microscope setup with high speed detector. The conventional quadrant photodiode is replaced with a fast position-sensitive detector system. Lens L1 is used to collimate the laser after the dichroic mirror. The fiber optic waveguide splitter splits the collimated incoming beam into two equal halves. The laser beams coming out of each arm at the back end of fiber splitter are collimated again by lens L2 and L3 respectively. Lens L4 and L5 focus the light into two single diodes on the detector.

mized. The first function is the splitting of the beam and the second function is the balanced photodetection with high gain and bandwidth. This was realized in practice with a fiber optic waveguide that was split into halves with the light from each end focused onto a fast photodiode [94]. The two detectors were operated in a balanced subtraction mode, providing position information along one lateral dimension. A schematic representation of our setup with the faster detector is shown in Figure 3.1. The detector (PDB120C, ThorLabs, USA) has two circular InGaAs-PIN photodiodes separated by a distance of 2 cm. Each photodiode has a diameter of 0.3 mm and is sensitive in the range of 800-1700 nm. Its sensitivity at 1064 nm is about 0.67 A/W. The differential amplifier of the detector has a bandwidth from DC to 75 MHz and a high transimpedance gain of 1.8×10^5 V/A.

The fiber optic waveguide splitter has the function to spatially split an incident laser beam in two equal halves. The front end of the bundle was sorted vertically, where two halves were separated at the back end of the bundle. The fiber splitter was assembled with 1000 multimode fibers (Model MM-S105/125-22A, 105 μm core, 125 μm cladding, Nufern Corporation, USA) packed into a 4.4 mm diameter front end with two back ends composed of an equal number of fibers. The fibers were stripped of their coating to allow a higher packing efficiency, which can reduce the loss of the incident laser beam. Stripping the protective coating exposes the fragile glass core and cladding, so heat-shrink tubing was used to bind and protect the exposed fiber tips. To permanently seal the fibers, low viscosity glue (Acrylic 609, anaerobic cure, Henkel Loctite Corporation, USA) was applied between the fibers. Two aluminum rings were glued over the front end to help mount the bundle for cutting and polishing. A diamond-edge blade was used to cut the fibers to the same length. After the fibers were cut, the fiber bundle tips were polished with a series of aluminum oxide lapping films of grits ranging from 30-0.3 μm (Model LFG, aluminum oxide lapping films: 30, 5, 3, and 0.3 μm, ThorLabs Corporation, USA).

After the waveguide splitter, additional optics was used to direct the two light beams into those separate photodiodes. Due to the numerical aperture of the fibers (NA=0.22), light coming out of the waveguide must be collimated and focused onto the balanced photodetector. We collimated the light from the back end of each bundle using two-inch diameter, 37 mm focal length aspheric lenses (lenses L2 and L3 in Figure 3.1). The collimation serves to redirect the light toward the balanced detector without any loss due to the divergence of the light coming out of the fibers. The collimated light is directed by successive mirrors toward the balanced detector. Finally two smaller aspheric lenses (one-inch diameter 12 mm focal length, lenses

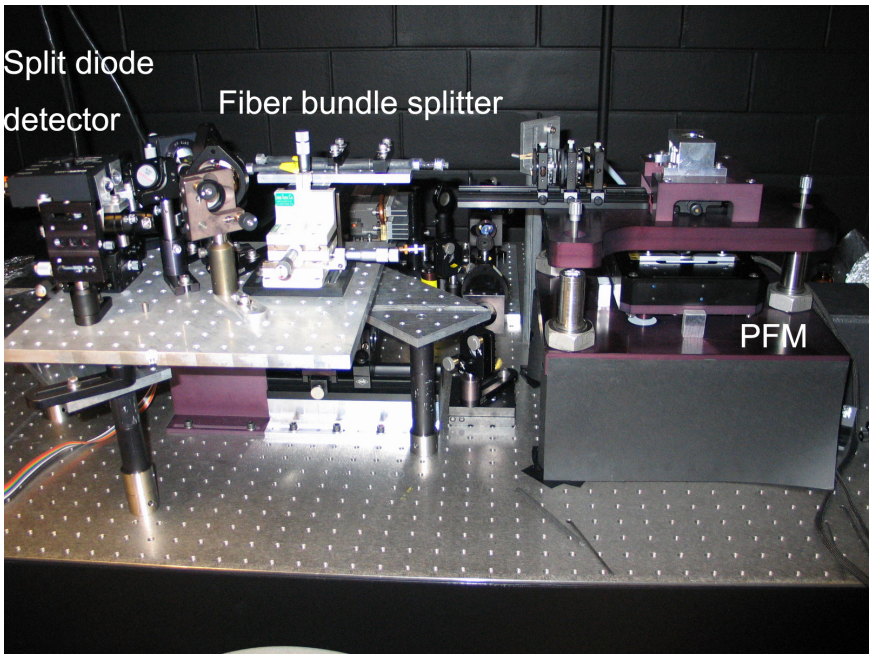

Figure 3.2: Image of the photonic force microscope with the high speed detector.

L4 and L5) focus the light onto the detector. Each of these lenses and the detector were mounted on translation stages for alignment and balancing.

The transmission efficiency of the fiber waveguide is determined by measuring the total power coming out of both arms and the power entering the waveguide. The transmission efficiency was determined to be 30% of the initial power of the incident laser beam. The fiber can only transmit light if the light impinges on the core of the fiber. Therefore light entering the cladding region of the fiber is lost. A loss of 29% is accounted for by the ratio of the cross-sectional area of the core to that of the total cross section of the fiber. The rest of the 41% is lost due to packing efficiency and broken fibers (five fibers were known to have broken out of 1000).

After the position detector system was assembled, it was integrated into the photonic force microscope, replacing the old quadrant photodiode. An image of the

setup is shown in Figure 3.2.

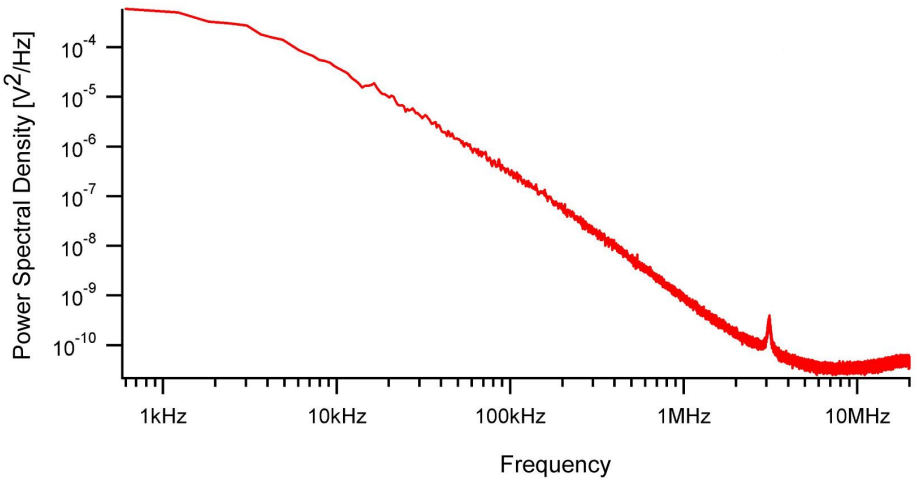

Figure 3.3: Power spectral density of the position signal of a 1 μm polystyrene particle trapped by the laser (IRCL-850-1064-S) from CrystaLaser. Position data was sampled at 40 MS/s for 100 ms. A resonance peak around 3 MHz shown on the power spectral density which is due to the high frequency laser noise.

To test the temporal response of our detector, we recorded the Brownian motion of a single particle moving within the optical trap. We used a high resolution high speed digitizer (14-Bit, DC to 100 MHz, PXI-5122, National Instruments, USA) to record data. All data was taken at a sample rate of 100 MS/s over a sampling time of 40 ms. The data was collected on the digitizer and transferred to the computer for analysis. Initially, the 1064 nm Nd:YAG laser from CrystaLaser (IRCL-850-1064-S, CrystaLaser, USA) was used to form the optical trap. However, a resonance peak at about 3 MHz due to the laser intensity fluctuation was found on the power spectral density of the position signal (see Figure 3.3). The amplitude of the laser noise at 3 MHz is much larger than the amplitude of true Brownian motion around this time scale. Therefore we changed to another 1064 nm laser with a maximum power of 700 mW (NPRO 126-1063-700, Lightwave Electronics (now JDSU), USA).

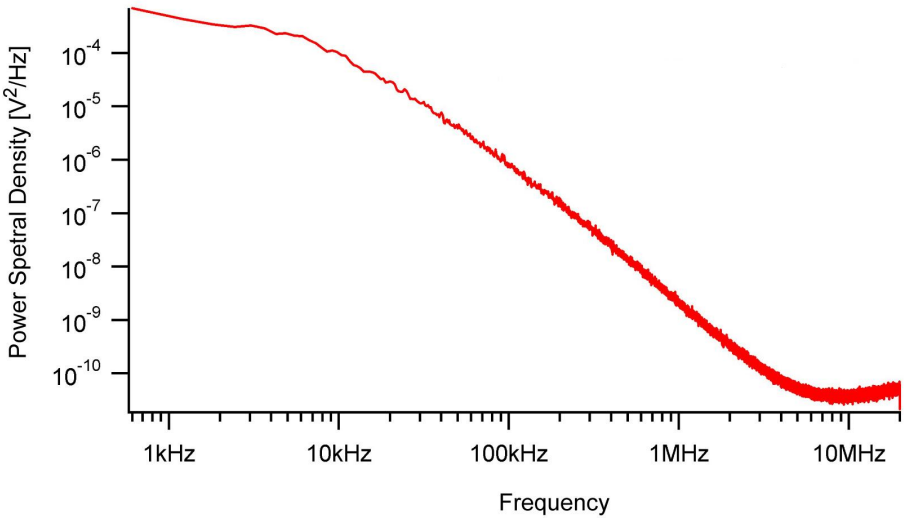

Figure 3.4: Power spectral density of the position signal of a 1 μm polystyrene particle trapped by the laser (NPRO 126-1063-700) from JDSU. Position data was sampled at 40 MS/s for 100 ms. No resonance peaks are seen up to a frequency of 20 MHz.

This laser has very low noises at frequencies up to 20 MHz as shown in Figure 3.4. Therefore, all experiments were performed with this laser.

Figure 3.5 shows the mean square displacement of a 1 μm polystyrene bead in water (red dots). The mean square displacement continues to increase starting at 20 ns and reaches a plateau value at around 100 μs due to the trap confinement. The first point on the curve at 10 ns is outside of the Nyquist frequency and should be discarded. For this curve, the y-axis shows the mean square displacement in units of nm^2 and the background noise is also given to show both the temporal and spatial resolution range of the detector. The background signal was recorded when a particle was not present within the optical trap at the same laser power. Basically, it consists of all the noises coming from laser power fluctuations, pointing instability, and electronic noises coming from the amplifier and the digitizer. The

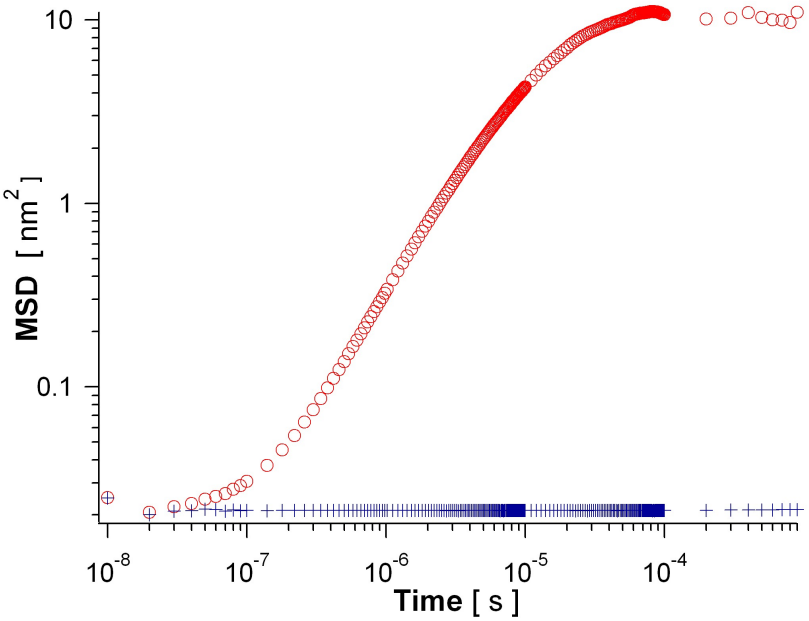

Figure 3.5: Mean square displacement of a 1 μm polystyrene bead in an optical trap (red circles) with the noise background shown (blue crosses). The temporal resolution of the detector is around 30 ns with spatial resolution of about 1 Å.

main noise source is actually the high frequency electronic noise since the mean square displacement of the background noise reaches the plateau very fast – within about 50 ns. The electronic noise generally does not correlate with the true signal induced by the displacement of the trapped particle. Thus the total measured amplitude x_{tot} can be expressed as

$$x_{tot} = x_p + x_e \tag{3.31}$$

where x_p is the true displacement of the trapped particle and x_e is the electronic

noise. The mean square displacement of the total signal is then calculated as

$$\begin{aligned} MSD_{tot}(\tau) &= \langle (x_{tot}(t+\tau) - x_{tot}(t))^2 \rangle \\ &= \langle (x_p(t+\tau) - x_p(t) + x_e(t+\tau) - x_e(t))^2 \rangle \\ &= \underbrace{\langle (x_p(t+\tau) - x_p(t))^2 \rangle}_{MSD_p(\tau)} + \underbrace{\langle (x_e(t+\tau) - x_e(t))^2 \rangle}_{MSD_e(\tau)} \\ &+ 2 \underbrace{\langle (x_p(t+\tau) - x_p(t)) \rangle}_{0} \underbrace{\langle (x_e(t+\tau) - x_e(t)) \rangle}_{0} \\ &= MSD_p(\tau) + MSD_e(\tau) \end{aligned} \tag{3.32}$$

Thus the mean square displacement of the true Brownian motion of the trapped particle could be obtained by subtracting the MSD of noise from the MSD of total signal. As we can see from Figure 3.5, the MSD from the total signal drops into the background noise at 30 ns, which corresponds to a mean square displacement below 0.03 nm^2, providing a spatial resolution in the 1 Å range [3]. This result was confirmed by measuring different sized polystyrene, silica and melamine resin beads where we found similar spatial resolution (see Table 3.1).

In general, the new detector achieves 30 ns temporal resolution and 1 Å spatial resolution on a 1 μm polystyrene particle, which is about 30 times faster than the quadrant photodiode detector previously used in the study of Brownian motion [93]. Although the detector has different temporal resolutions for different particles due to different detector sensitivities, all temporal resolutions are better than τ_p with a minimum of $0.2\tau_p$ for a 3.5 μm silica particle, which renders the detector capable of studying the Brownian motion at the time scale of ballistic motion which has never

[3] This resolution basically defines how well we can measure the mean square displacement for a Brownian particle. It is not the same thing as the resolution in single particle tracking, e.g. how well one can resolve the position of the center of the particle.

Table 3.1: Spatial and temporal resolutions for different particles

Particle Diameter [μm]	Spatial resolution [Å]	Temporal resolution [μs]	τ_p [μs]
0.5	0.84	0.02	0.015
1	0.52	0.03	0.058
2.5	0.63	0.14	0.36
3.5	0.61	0.22	0.71
1	0.83	0.06	0.11
2.5	0.95	0.26	0.68
3.5	0.66	0.28	1.34
2	1.1	0.2	0.34
3	0.85	0.28	0.98

*Blue—Polystyrene; Red—Silica; Green—Melamine Resin

been possible before.

3.3 Experimental investigation of Brownian motion at fast time scales on a single particle

A schematic representation of the experiment is shown in Figure 3.6. While a nanometer- or micrometer-size particle undergoes Brownian motion within the optical trap, its position time trace is recorded with the high bandwidth detector just described. The particle's concentration is diluted to about 1 particle per $200 \times 200 \times 200$ μm volume. This low concentration avoids hydrodynamic interactions between particles and trapping multiple particles during the experiment. Larger particles (diameter$>$ 2 μm) usually sediment very fast so that all the particles settle down on the bottom coverslip soon after the sample is prepared. In this case, the optical trap will be first brought to the coverslip and moved back again into the solution after it catches one particle. The trapped particle is kept away from the bottom coverslip with a distance at least 10 times greater than the par-

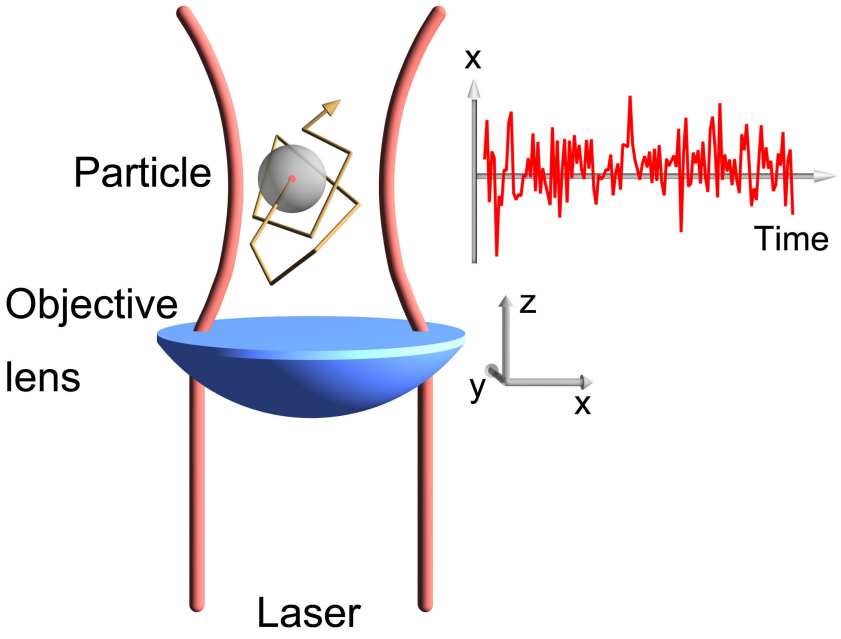

Figure 3.6: Experimental scheme for Brownian motion at fast time scale. A single nanometer- or micrometer-size particle is confined by an optical trap to the detection area. While the particle undergoes Brownian motion within the trap, its position time trace along one lateral dimension is recorded with a high bandwidth position detector.

ticle's diameter, typically 30 μm, at which the hydrodynamic interaction between the particle and the bottom coverslip can be negligible. The detector output is recorded with the high bandwidth digitizer at 100 MHz for 40 ms per segment while the particle is moving in the trap. The length of the data segment is limited by the on-board memory of the digitizer. For calculating the velocity autocorrelation function, multi data segments (100 segments for 4 seconds in total) on the same particle were recorded for averaging.

3.3.1 Brownian motion influenced by the hydrodynamic memory effect

We can rewrite Equation (3.19) in a normalized form as

$$\frac{\langle[\Delta x(t)]^2\rangle}{2Dt} = 1 - 2\sqrt{\frac{1}{\pi}\frac{\tau_f}{t}} + \frac{8}{9}\frac{\tau_f}{t} - \frac{\tau_p}{t} + \Omega(\frac{\tau_p}{\tau_f}, \frac{t}{\tau_f}) \tag{3.33}$$

so that the right hand side of the equation is a function of τ_f, ρ_f and ρ_p since $\tau_p = \frac{2\rho_p}{9\rho_f}\tau_f$. It is easy to see that for particles with same density but different radii immersed in the same liquid medium, their normalized MSD would collapse into one curve if t is also normalized to τ_f. Figure 3.7 shows the normalized MSD calculated from single data segments of three different polystyrene spheres (Diameter=1, 2.5 and 3.5 μm). The data was fitted with Equation (3.33) for times t from $0.01\tau_f$ to $2\tau_f$, spanning about 2 decades. The theoretical fit has two fitting parameters that correspond to the radius of the particle and the detector's sensitivity (see Appendix A). The theory agrees with the data very well within 3%. This agreement with theory has been extended to the time scale of $0.01\tau_f$, which is two orders of magnitude smaller than previous experiment [93]. It is also interesting to see that the time evolution of the normalized MSD is completely determined by only one

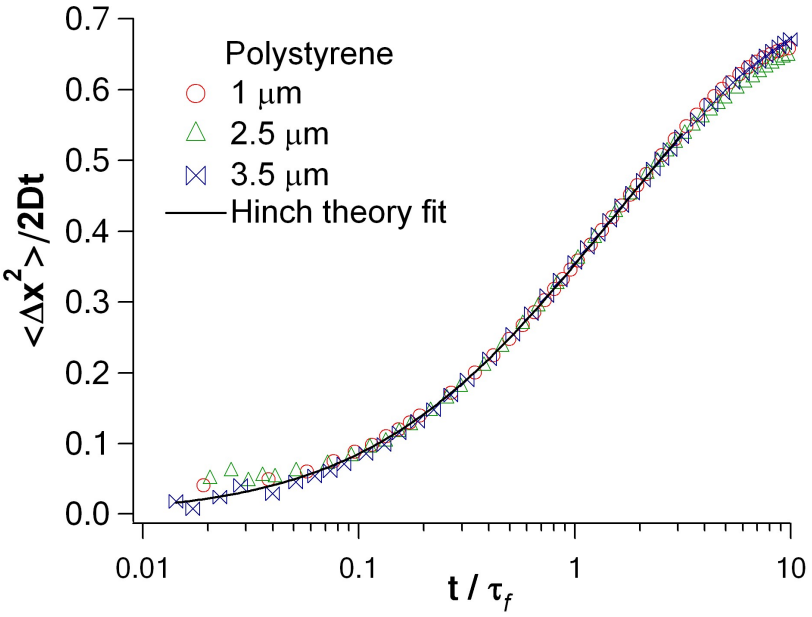

Figure 3.7: The overlap of normalized mean square displacements for polystyrene particles with diameters of 1, 2.5 and 3.5 μm indicates the hydrodynamic memory effect. Mean square displacement was normalized to its value at free diffusion regime $2Dt$ and the time was normalized to the characteristic time scale of hydrodynamic memory effect τ_f, which are 0.25, 1.56 and 3.06 μs for 1, 2.5 and 3.5 μm polystyrene particles respectively.

simple parameter – the characteristic time scale of the hydrodynamic memory effect τ_f.

3.3.2 Brownian motion dominated by the particle's own inertia

Figure 3.8 shows the normalized MSD for silica (ρ = 1.96 g/ml) and polystyrene (ρ = 1.06 g/ml) particles of the same size (diameter= 2.5 μm). The MSD has been normalized to the value at the random diffusive regime $2Dt$, and the time axis has been normalized to τ_f. Both particles do not show random motion at the time scale since their normalized MSD values are way below 1. The two curves overlap

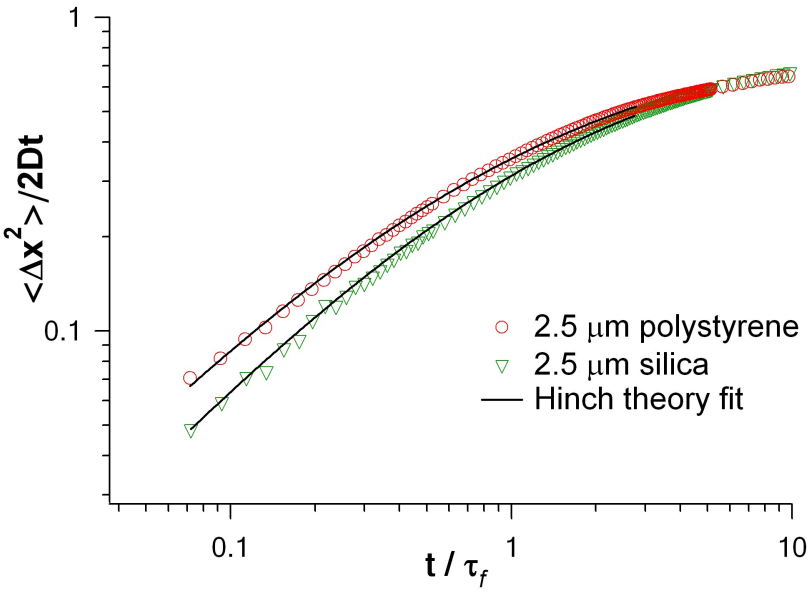

Figure 3.8: Normalized MSD for 2.5 μm silica (1.96 g/ml) and polystyrene (1.05 g/ml) particles. The time scale is normalized to τ_f, and the MSD is normalized to the value at free diffusion regime $2Dt$. Deviation of MSD for same sized particles with different densities indicates the inertia effect of the particle.

at times $t > 3\tau_f$ and separate more as they approach shorter time regimes. This digression is an indication of the particle's inertia effect on its motion. Both silica and polystyrene particles have the same diameter and displace the same amount of fluid, thus the fluid inertia effect acts equally on the particles. However, the silica particle has a higher density than the polystyrene particle, so on average it moves slower after receiving the impulse from the surrounding water molecules. The difference on MSD values is discernable right below $3\tau_f$, and becomes more obvious towards shorter time scales. At the resolution limit of 0.07 τ_f, the normalized MSD for the polystyrene particle is about one times greater than that of the silica particle, which shows that the inertia of the particle completely dominates the motion at this time scale. At times above $3\tau_f$, the two curves overlap, indicating that the particle's inertia effect dies out and the motion slower than $3\tau_f$ is completely dominated by the fluid inertia.

3.3.3 Ballistic Brownian motion

Figure 3.9 shows the MSD normalized to the value at the ballistic regime $\frac{k_B T}{m^*} t^2$ for silica particles with different sizes. For a 1 μm silica particle, the temporal resolution is very close to $\tau_p = 0.1$ μs, but for a 2.5 μm silica particle, the temporal resolution is far smaller than $\tau_p = 0.68$ μs reaching about $0.3\tau_p$. The maximum normalized value reaches 90% for a 2.5 μm silica particle, indicating that the observed Brownian motion is approaching the ballistic motion that maintains a constant velocity. In the ballistic regime, Brownian motion preserves its directionality and magnitude of the momentum after the particle receives the impulse.

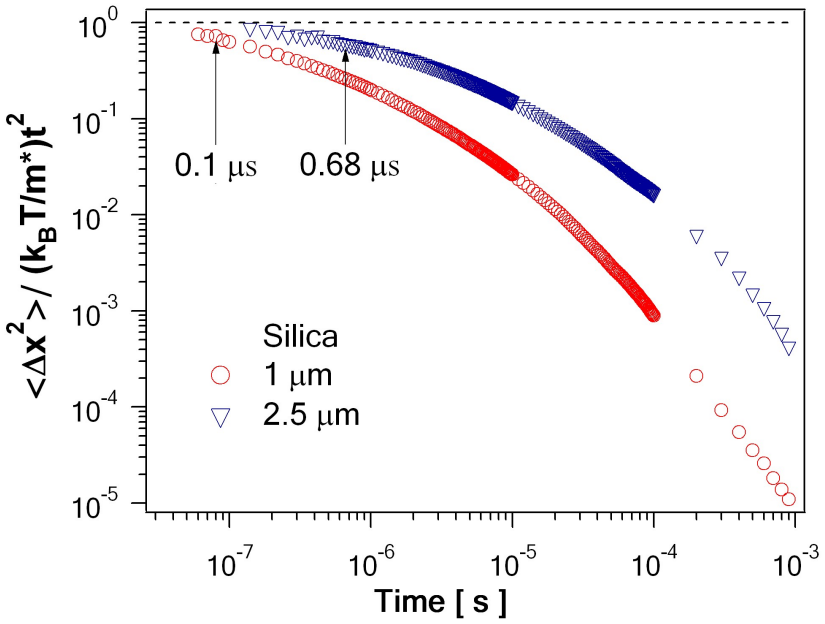

Figure 3.9: Normalized mean square displacement for 1 and 2.5 μm silica particles shows how well the particles' motion approaches the ballistic regime. Mean square displacement is normalized to its value at the ballistic regime $\frac{k_BT}{m^*}t^2$.

3.3.4 The velocity autocorrelation function of a Brownian particle

As we all know, a random path is a non-smooth curve and therefore non-differentiable. The velocity of a Brownian particle is unobtainable if its motion is observed at the time scale of random motion. This is not a problem for the ballistic Brownian motion. Figure 3.10 shows the velocity autocorrelation function [4] of a 2 μm melamine resin particle in water. The corresponding characteristic time scales for a 2 μm melamine resin particle are $\tau_p = 0.336$ μs, $\tau_f = 1$ μs and the autocorrelation time for the optical trap is $\tau_k = 59.9$ μs. At the short time scale around τ_p, the velocity autocorrelation function decays approximately exponentially, and is then followed by a power law decay around τ_f. Negative correlations are present at the time scales between 15 μs to 300 μs. This negative correlation is a result of the restoring force in the harmonic potential that tries to pull back the particle when it is displaced away from the potential minimum. The data has been fitted with Equation (3.26) for a Brownian particle moving in a harmonic potential in the Stokes-Boussinesq friction limit for times t from 0.2 μs to about 2 ms. The data agrees with the theory very well in the entire time domain spanning four decades in which the particle's motion is dominated by different effects.

To our knowledge, this is the first experimental velocity autocorrelation curve given for a Brownian particle down to the time scale of τ_p. Due to the convolution of high frequency electronic noise, direct measurement of the velocity of the particle is still not practical with the current spatiotemporal resolution of the setup. However, in the process of calculating the velocity autocorrelation function, this uncorrelated random electronic noise can be averaged out, giving the true time evolution of the velocity autocorrelation of the Brownian particle. The excellent agreement with the

[4] For the calculation of the velocity autocorrelation function, refer to Appendix B

theory indicates that the continuum hydrodynamic model still works down to the time scale of τ_p.

3.3.5 Discussion and summary

We have developed a novel detector that circumvents the bandwidth limits of the conventional position-sensitive quadrant photodiode. This detector provided a temporal resolution of 30 ns in the observation of the Brownian motion of single 1 μm polystyrene particles, which surpassed the resolution of conventional QPD by more than one order of magnitude. In the study of particles with various densities and diameters, the temporal resolutions were always better than the characteristic time scale τ_p, making it possible to study the particle's inertia effect and observe Brownian motion at the ballistic regime.

The inertia effect of the particle and the fluid have been studied on single particles with different sizes and densities, and ballistic motions of the Brownian particle have been observed. The time evolution of normalized MSD $\langle[\Delta x(t)]^2\rangle/2Dt$ for polystyrene particles of different sizes are shown to be governed by the characteristic time scale τ_f. The particle's inertia effect on Brownian motion has been clearly shown for 2.5 μm silica and polystyrene particles. The continuum hydrodynamic theory on Brownian motion has been verified down to the time scale smaller than τ_p, which extended more than two orders of magnitudes towards shorter time scales than previous experiments. For the first time, the velocity autocorrelation function of a single Brownian particle was obtained and we found an excellent agreement with the Clercx theory over the entire time region for motions dominated by either inertia effects or the harmonic potential.

Due to the high frequency noise contained in the position signals, we could

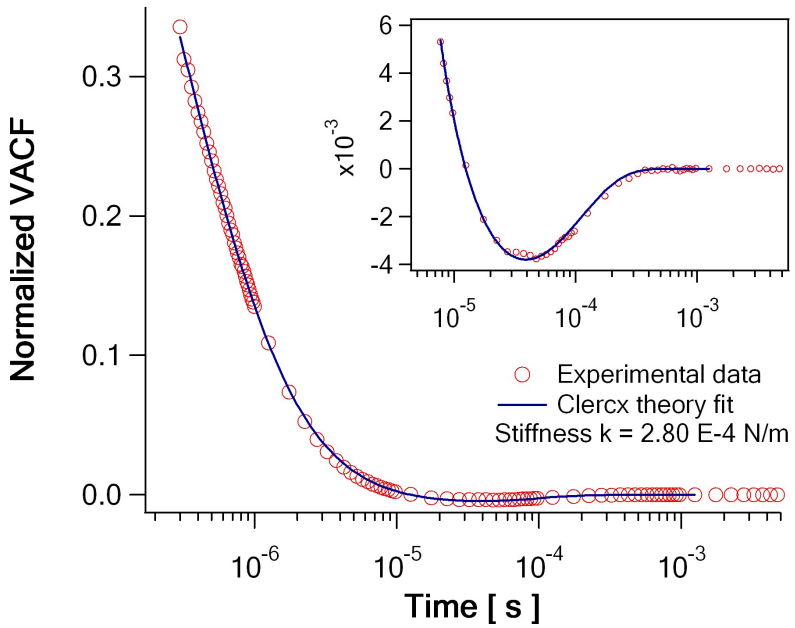

Figure 3.10: Velocity autocorrelation function of a 2 μm melamine resin particle in an optical trap. The velocity autocorrelation function was normalized to k_BT/m^*, where m^* is the effective mass of the particle. The spring constant of the trap is 2.80×10^{-4} N/m, which was calibrated from a 10 second time trace sampled at 50 KHz. The calculated velocity autocorrelation function was averaged over 100 data segments with each segment sampled at 50 MHz for 80 ms. The data above 1 μs was blocked to 20 points per decade for fitting and display. The solid line shows that Clercx theory fits the whole experimental velocity autocorrelation function. The fit includes a calibration factor as the only fitting parameter. Inset shows the negative correlation induced by the confinement of the optical trap.

not obtain the real time evolution of the velocity of the Brownian particle with our current instrument. We are looking for ways to minmize these noises. With an increased signal-to-noise ratio, the velocity time trace could be obtained directly from a position time trace when the motions are observed in the ballistic regime. If that is possible, one can carry on many fundamental studies on a single Brownian particle, for example, confirming the equipartition theorem for a Brownian particle that has been assumed in theoretical derivations but has never been directly proven experimentally. Another benefit of improving spatiotemporal resolution in the observation of Brownian motion is that we could directly study the relaxation process happening at the time scale of sound propagation τ_c due to the compressibility of the fluid. Our data shows clearly that at time scales $t \geq \tau_p$, the effective mass $m^* = m + \frac{1}{2}m_0$ can describe the particle's motion extremely well. However, the details of this relaxation process have never been accessed before. For a 1 μm particle, τ_c is about 1 ns, which is about 30 times smaller than our current resolution.

Appendix A: Fitting mean square displacement with Hinch theory

Since the time scale is far below τ_k, the data can be fitted with Hinch theory for a free Brownian particle. MSD given by Hinch is as follows:

$$\frac{\langle[\Delta x(t)]^2\rangle}{2Dt} = 1 - 2\sqrt{\frac{1}{\pi}\frac{\tau_f}{t}} + \frac{8}{9}\frac{\tau_f}{t} - \frac{\tau_p}{t} + \frac{3}{t(5\tau_f - 36\tau_p)^{1/2}} \times \left(\frac{1}{\alpha_+^3}e^{\alpha_+^2 t}erfc(\alpha_+\sqrt{t}) - \frac{1}{\alpha_-^3}e^{\alpha_-^2 t}erfc(\alpha_-\sqrt{t})\right)$$

where $\alpha_\pm = \frac{3}{2}\frac{3\pm(5-36\tau_p/\tau_f)^{1/2}}{\sqrt{\tau_f}(1+9\tau_p/\tau_f)}$, $\tau_p = \frac{m}{\gamma}$ and $\tau_f = \frac{\rho_f r^2}{\eta}$. The fit includes two fitting parameters, a particle radius r and a calibration factor C that converts voltage to nanometers. Weighted least square with standard deviation is chosen as the fitting method. This weighted method greatly increases the stability of fitting. Measurements have been done on silica, polystyrene and resin particles of various sizes. Hinch theory fits the data in the free diffusion region very well for all the particles we have tested. The particle radius from the fit falls in the size range given by the manufacturer for silica particles. For polystyrene and resin particles, the average fitted particle radius is about 10% larger than the specified mean particle size. It is possibly because the polymer particles swell in water with water molecules penetrating into the particle surface and thus increase its effective size. The fitting with these two parameters is the best method to use to find their true values, since the particle radius and the calibration factor are closely related. In the other optical tweezers calibration methods, one needs to assume the particle radius as the mean radius given by the manufacturer. This is obviously not precise due to the increase of effective radius for polymer particles.

Appendix B: Calculation of the velocity autocorrelation function

The time series of the position traces are sampled at 50 Mhz in the resin particle experiment. However, the temporal resolution on the 2 μm resin particle is about 5 Mhz. Therefore, high frequency noises are contained in our measurements. A box car smooth with size of 10 points is applied to the data to get rid of the high frequency noise above 5 Mhz. The velocity autocorrelation function is calculated on this smoothed data trace and an average velocity autocorrelation function is then obtained from 100 data traces sampled consecutively from the same particle. The length of a single data trace is limited to the onboard memory on our digitizer. We can only record 4 million points on a single shot. Averaging would not be necessary if we could record a much longer time trace.

Chapter 4

Thermal Noise Imaging on large scale objects

This chapter presents our latest developments of thermal noise imaging that uses thermal motion as a "natural scanner" to probe three-dimensional nano structures. Thermal noise imaging is the first real three-dimensional scanning probe microscopy with powerful applications in imaging soft materials. However, thermal noise imaging for large scale imaging is a long process, which limits its application to real biological problems. We devised a novel way to combine conventional point-to-point scanning (raster scan) with thermal noise imaging, which has improved imaging efficiency more than 40 times. This development should promote wider applications of thermal noise imaging in biological research.

4.1 Introduction and Motivation

Scanning probe microscopy (e.g. Atomic Force Microscopy (AFM) and Scan Tunneling Microscopy) has been very successful in investigating structures at atomic and

molecular scales by scanning a sharp tip point-to-point on surfaces with nanometer or better resolutions [95, 96]. It has been used to image individual atoms on crystal surfaces, molecules on hard substrates, nanometer or micrometer lithographic patterns, and even interactions at the atomic and molecular level [97–99]. However, when it comes to biological applications in which imaging soft materials in three dimensions is crucial, e.g. cytoskeleton inside a cell, the mechanical contact between the tip probe and the microscope frame poses insurmountable difficulties. The limitations on the mechanical contact are two fold: (1) the forces generated by the atomic force microscope are typically too high for imaging soft materials; (2) the probe can not go into a three-dimensional object without disrupting the materials or breaking its link to the mechanical frame of the microscope.

4.1.1 An optically trapped particle as a probe in scanning probe microscopy

Using an optically trapped particle as a scanning probe is potentially a more promising approach for developing a true three-dimensional scanning probe microscope for soft materials. Trapping particles by using a focused laser beam eliminates the mechanical connections between the probe and the microscope frame, which allows the probe to go inside the materials and image the three-dimensional structures. Also due to the weak light-matter interaction, the force applied by the probe on the soft materials can be on the order of thermal forces, preventing distortions and damage to the soft materials. The spring constants of optical traps typically range from 10^{-4} to 10^{-6} N/m, which are 2 to 4 orders smaller than those of AFM.

The idea of using an optically trapped particle as a scanning probe was first proposed by Malmqvist and Hertz in 1992 [100]. The major difficulty encountered

was how to monitor the particle's position while scanning, especially the position along the optical axis since that contains the most direct and important information relating to the profile of the scanned surface. Ghislain and Webb monitored the forward scattered light intensity from a trapped glass shard to measure the displacement of the shard as it scanned over a photoresist surface [101]. They claimed that their forward scattered light method could resolve features as small as 20 nm. Malmqvist and Hertz trapped nonlinear crystal $LiNbO_3$ particles between 50 and 100 nm in diameter with a 1064 nm infrared laser beam and used the frequency doubled visible light emitted from the particle to image the sample in the near-field [102]. The samples were limited to those with strong absorption in the visible light range but almost transparent in the infrared range so that the transmitted visible light through the sample was inversely proportional to its thickness. Their experimental resolution was limited to about 500 nm, but the theoretical resolution of this technique should be limited to the size of the particle and the amplitude of its Brownian motion. A similar imaging method was also explored by Kawata *et al.* [103]. Florin *et al.* used the intensity of the two-photon fluorescence of an optically trapped 200 nm latex particle to measure the particle's axial displacement, and used this technique to image biological samples (hippocampal neurons) fixed on a glass coverslip for the first time [104, 105]. This detection technique achieved about 40 nm resolution in the axial direction, and its lateral resolutions were also limited to the size of the particle. Friese *et al.* employed the backscattered light from the trapped particle to determine the average axial position of the particle [106]. They claimed that the technique achieved a sensitivity of 5 nm in the height measurement. In their experiment, a feedback control based on the backward scattered light level was also incorporated for the first time for the trapped particle microscopy. Although they

claimed to be three-dimensional scanning, all of the above mentioned experiments were actually AFM-like two-dimensional surface scanning since they did not scan along the axial direction. The development of an actual three-dimensional scanning microscope came after the three-dimensional detection method (laser interferometry using forward scattered light [35]) was invented.

4.1.2 Thermal noise imaging: using thermal motion as a "natural scanner"

As described earlier, the laser interferometry detection method allows for detection of the particle's displacement relative to the trapping center with nanometer or better resolution in all three dimensions. This superior detection method helped researchers realize that the traditional point-to-point scanning scheme would not be able to achieve high resolution due to the particle's Brownian motion. For a particle confined in an optical trap with a spring constant of $k = 10^{-5}$ N/m at room temperature, its amplitude of Brownian motion can be estimated to be about 20 nm by

$$\Delta x = \sqrt{\frac{k_B T}{k}} \tag{4.1}$$

where k_B is the Boltzmann constant and T is the temperature. As shown in Figure 4.1, the amplitude of thermal motion can even reach up to a couple hundred nanometers for weaker optical traps.

The thermal motion of the trapped particle pose fundamental limits when the probe has to be fixed at one point during scanning for achieving a high resolution. However, it did not take too long to realize that the disadvantage of thermal motion can actually be turned into an advantage [55, 107]. The Brownian motion of the probe particle could be used as a "natural scanner" that probes nanostructures

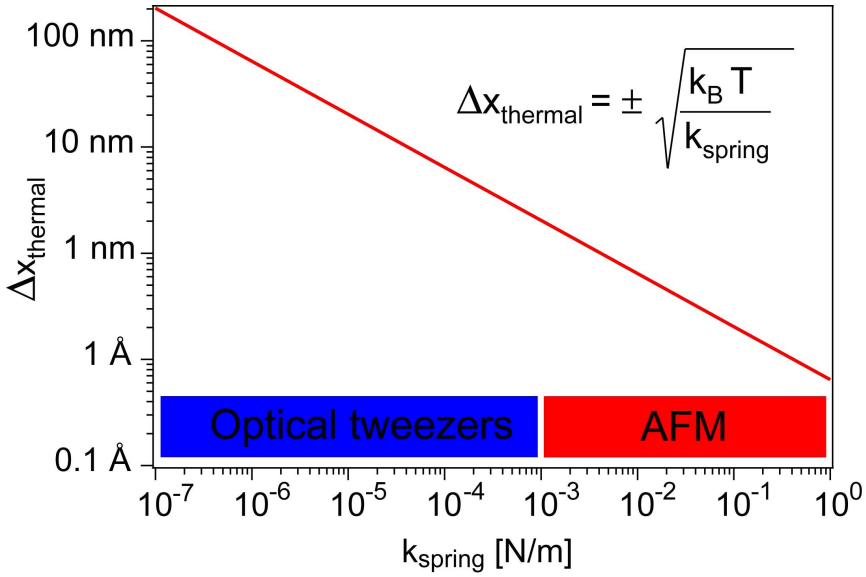

Figure 4.1: Residual thermal fluctuations of the sensor as a function of the stiffness of the sensor.

randomly in three dimensions, a process that is very efficient on the nanometer scale. This phenomenon of using Brownian motion to explore short range targets is indeed very common inside a cell. For example, small signalling molecules explore their binding sites on target molecules through simple diffusion at the last several tens of nanometers after they are directly transported to the proximity of the target molecules by molecular motors.

In this imaging mode, the optical trap is only required to confine the particle to the volume of interest which it explores by diffusion. Subsequently, images of objects which come into contact with the diffusing probe are computed from the probe's three-dimensional (3D) position traces. A 3D histogram of probe positions shows how often the probe visits a certain volume element during data acquisition. To scan a larger volume, the position of the trap would be scanned in three dimensions while enough time is allowed at each position for the particle to completely

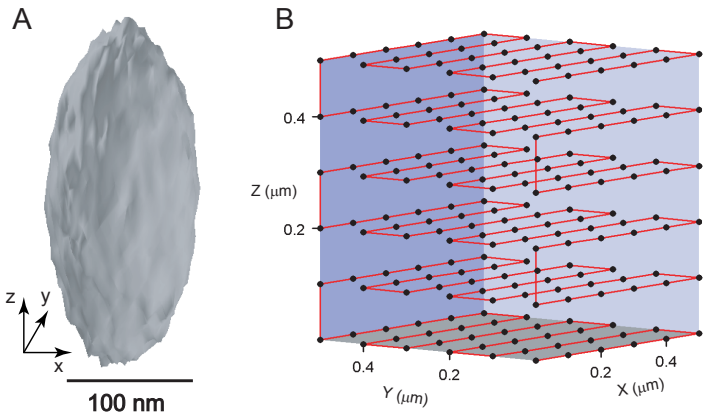

Figure 4.2: Illustration of 3D thermal noise imaging. A) shows the isosurface at 5 counts of the 3D position histogram at one individual trap position for a 200 nm diameter polystyrene particle sampled at 50 KHz for 3 seconds. B) indicates the scanning path using thermal noise imaging to explore a volume larger than an individual trapping volume. Each black dot represents the trap center during the scanning.

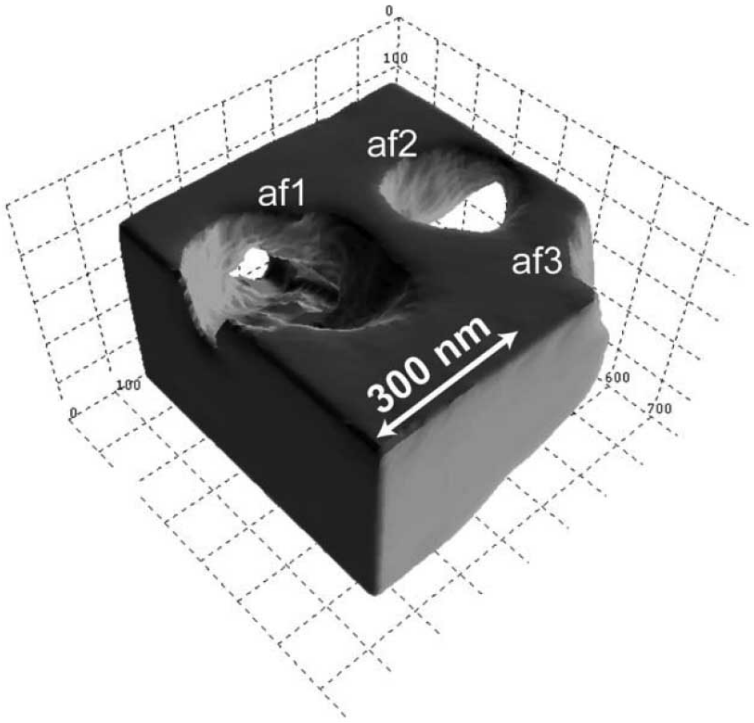

Figure 4.3: 3D thermal noise image of agar gel (figure reproduced from [55]). Vacant spaces in the graph indicate the volume occupied by agar filaments.

explore the accessible volume. The final image is then the sum of all 3D position histograms at each trap position. The scheme of thermal noise imaging is shown in Figure 4.2. As the probe cannot explore volume elements occupied by solid objects, the resulting 3D position histogram contains excluded volumes. For instance, polymer filaments of an agar gel appear in such a histogram as channels as shown in Figure 4.3 [55]. We call these 3D histograms "thermal noise images" and the imaging method "thermal noise imaging".

The spatial resolution in thermal noise imaging is no longer limited by thermal fluctuations of the probe but by the quality of the position histograms, i.e. the frequency with which the particle visits the same volume element during data ac-

quisition and the binning of the histogram. Typically, a voxel [1] size of 10 nm that is much larger than the resolution of the laser interferometry detection method is used in thermal noise imaging. A thermal noise image is displayed as the isosurface at a certain number of counts in each voxel of the 3D position histogram. A significant isosurface value with small statistical noises can be estimated from Poisson statistics. For example, Figure 4.3 displays the isosurface at 5 counts per voxel. The probability of obtaining ≤ 5 counts in a voxel that does not have any objects by statistical fluctuations is given by

$$\sum_{n=0}^{n=5} \frac{e^{-m} m^n}{n!} = 0.00279 \quad \text{for} \quad m = 15 \ ^{2} \tag{4.2}$$

which is less than 1%. The confinement of the particle by the optical trap ensures that the probe particle stays in the volume of interest and samples it with sufficient frequency to achieve nanometer spatial resolution.

4.1.3 Limitations on thermal noise imaging and our motivation

Although thermal noise imaging is very efficient on the nanometer scale, scanning larger objects using thermal noise imaging is very time consuming, which limits its applications to practical biological problems. As we can see in Figure 4.3, in the scanned volume of about $600 \times 600 \times 400$ nm, only portions of individual agar filaments are visualized. From the image, little can be learned about the architecture of the polymer networks within the agar gel. However, in most cases, visualizing how individual polymers are connected in three dimensions is very important to learning about their properties, especially for constructing a theory addressing how

[1] A voxel is the 3D equivalent of a pixel (2D) or a bin (1D).

[2] The particle visited each voxel ≥ 15 times when there is no objects in the trap from a reference measurement [108].

the macroscopic mechanical properties of polymer networks arise from their three-dimensional architectures and mechanical properties of individual polymers [109, 110]. This would require thermal noise imaging of a much large volume, e.g. in micrometer scales. However, probing larger structures requires recording the particle position histograms at an increasingly higher number of trap locations that scales as d^3, where d is the characteristic linear dimension of the imaged volume. Such a process can be very time consuming. For example, scanning a 500 nm cube that requires a combination of 216 trap locations takes approximately 4 minutes. Doubling the size of the imaged region to 1 μm results in image acquisition time of approximately half an hour. However, scanning a 3 μm cube that might cover several pores of the network and help us to resolve the connection of an individual filament to its nearby neighbors, will take formidable 14 hours. It is very difficult and almost impossible to maintain the stability of the setup over such a long period of time. The fluctuations of laser intensity, evaporation of the liquid medium of the sample and the immersion fluid for an objective lens, and changes of room temperature etc. can cause unpredictable drifts and changes in the detector signal, which makes experiments spanning a long time impossible. Thus, we were inspired to invent a more efficient method for the application of thermal noise imaging of large scale objects.

4.2 An efficient imaging strategy for Thermal Noise Imaging

4.2.1 Basic principles

In most biopolymer solutions, the volume occupied by biopolymer filaments is typically less than 10%, and the rest of void is filled with liquid medium. Doing thermal noise imaging within such materials requires that a great portion of imaging acquisition time be wasted on a large vacant volume. Therefore, our idea for an efficient imaging strategy is to combine the traditional raster scanning that can quickly scan through the vacant volume with thermal noise imaging at the proximity of objects. The idea is comparable to the strategy used inside a cell: a combination of long range transport facilitated by molecular motors and short range transport through simple diffusion.

The objective of the raster scan is to quickly explore the vacant volume and register the positions of the objects within the volume of interest. One efficient way to achieve this is to start the raster scanning at the vacant volume[3] and then scan to both sides of this volume. When either the particle senses an object or reaches the boundary of the predefined scanning volume on one side, the trap is moved back to the starting position and then scans to the other side, which finishes one line scan as illustrated in Figure 4.4. A plane scan includes multiple such line scans with suitable stepsizes, and a volume scan will be a combination of multiple plane scans within the predefined volume. Thermal noise imaging can be either turned on when the particle senses the object, or after the raster scan has finished scanning the

[3]The position can be chosen when no obvious confinements on the three dimensional real-time traces of the trapped particle are seen. Usually, the calibration of the optical trap is also done at this position when the particle is free.

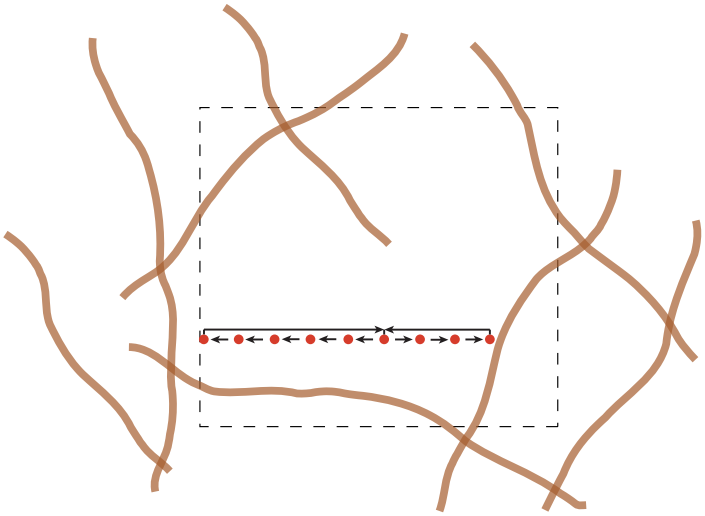

Figure 4.4: Illustration of a line raster scan within polymer networks. Red dots indicate each trap position during the scan. Dashed rectangular indicates the chosen volume for scanning. Arrow lines show the scanning path in a line raster scan.

whole volume and the positions of the objects are registered. The later is a better choice for two reasons. First, one can use a bigger particle for the raster scan since the maximum optical force is higher on bigger particles at the same laser power so that it can be moved with faster speed without losing it. In the later thermal noise imaging mode, the probe particle can be switched to a much smaller particle because it diffuses faster within the trap, which will drastically reduce the dwelling time at each trap position. Since the diffusion constant is inversely proportional to the particle's radius, a particle of 200 nm in diameter should in principle reduce the dwelling time by 5 times compared to a 1 μm particle. The smaller particle also gives much better resolution in thermal noise imaging. Second, after a large scale image of the objects is obtained via raster scan, thermal noise imaging can be only applied to the regions we are interested in without the need to sample all objects with TNI, which can save a great portion of image acquisition time for meaningful

data. In all experiments described here, thermal noise imaging was applied after the raster scan was finished on the whole volume.

This raster scan scheme can only explore one void at a time. For exploring a volume that consists of several voids, one must apply raster scan at each individual void and then combine the results for a complete image of that volume. Designing a raster scanning path for exploring multi voids at one time in three dimensions is a complicated problem and still under development.

For a trapped particle to sense an object and retract to its starting position, a feedback control system is needed. However, before we discuss the feedback control system, we'll need to explain our experiment apparatus and the sample.

4.2.2 Experimental setup

All the scanning experiments were done in the photonic force microscope as described in Chapter 2 where a conventional quadrant photodiode was used for the three-dimensional position detection of the trapped particle. The sample was prepared in a fluid cell that was mounted on the three-axis scanning stage. The fluid cell is a stainless steel disk with a center hole of 15 mm in diameter and a thickness of 0.8 mm. The fluid cell was enclosed by two circular coverslips from the top and the bottom. A polydimethylsiloxane (PDMS) microfluidic channel sample was firmly attached to the top coverslip by double-sided tape, with its patterned side facing the bottom coverslip. The distance of the patterned surface to the bottom coverslip was kept at about 10 μm, which is within the working distance of the oil immersion objective lens. Since the PDMS sample has a refractive index of about 1.40, 52% glycerine water solution was used to match the refractive index of the aqueous medium and the PDMS sample. Achieving the best refractive index match between

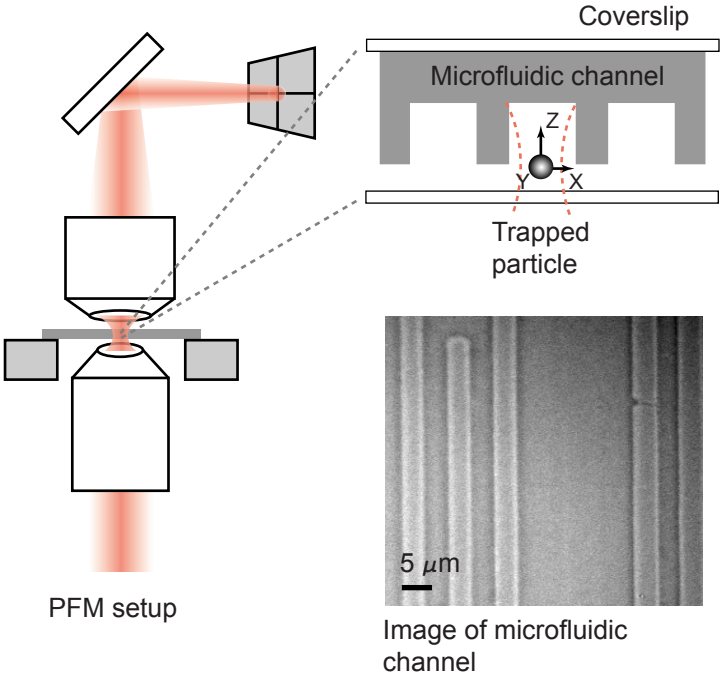

Figure 4.5: Layout and bright field image of the PDMS sample in the photonic force microscope. The particle is trapped at the focus of an objective lens and its three-dimensional position with respect to the trap center is monitored by the quadrant photodiode. PDMS microfluidic channel as the model sample is tightly adhered to the top coverslip with its patterned surface hanging about 10 μm from the bottom coverslip. The long rectangular channels have a typical width of 5 μm and a typical depth of 2 μm. The origin of the coordinate system XYZ is the center of the optical trap.

the PDMS sample and the aqueous medium is critical for three-dimensional position detection, in which any additional scattering of laser lights at the interface may cause artifacts in position signals. As we can see from Table 4.1, the refractive index of glycerine water solution highly depends on the amount of glycerine contained in the solution, which makes it a good option as a liquid medium with a tunable refractive index. The solution also contained two sizes of fluorescent polystyrene particles with 1 μm and 200 nm in diameter respectively. The concentration of the particles is controlled to have on average 1 particle per $20 \times 20 \times 20$ μm cube to avoid the trapping of multiple particles during scanning.

Table 4.1: Refractive Index of Glycerine Water Solutions

Glycerine% by Weight	Refractive Index	Glycerine% by Weight	Refractive Index
60	1.41299	50	1.39809
59	1.41150	49	1.39660
58	1.41001	48	1.39513
57	1.40852	47	1.39368
56	1.40703	46	1.39227
55	1.40554	45	1.39089
54	1.40405	44	1.38953
53	1.40256	43	1.38818
52	1.40107	42	1.38683
51	1.39958	41	1.38548

4.2.3 Developments of a feedback control system

To implement a raster scanning scheme, a signal that indicates the presence of an object is needed. Signals from QPD provide the three dimensional position of the trapped particle relative to the trap center. The origin of this coordinate system overlaps with the center of the trap. As we all know, a trapped particle is constantly undergoing thermal motions within the trap volume. If the trap volume is free of

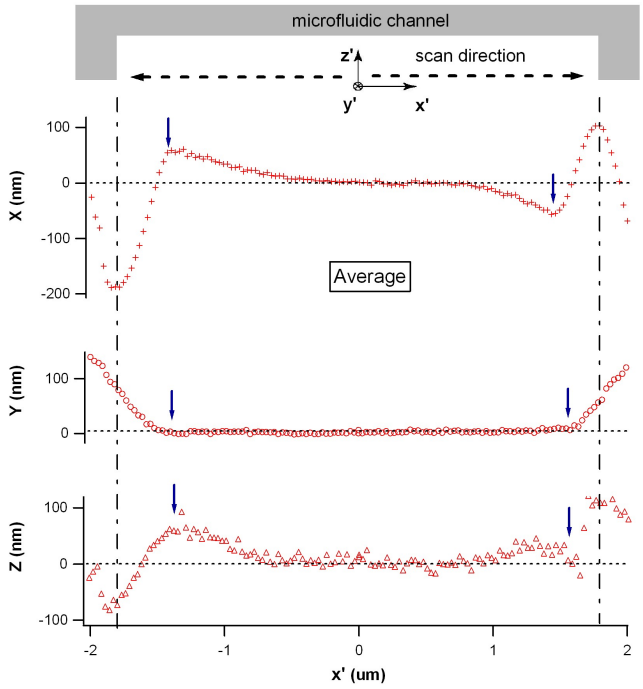

Figure 4.6: Average position of a 1 μm trapped polystyrene particle with respect to the trap center when the trap scanned across a microfluidic channel. Step size was 30 nm and the data was sampled at 100 Khz for 5 ms at each trap position. The spring constants of the trap are $k_x = 2.78 \times 10^{-5}$, $k_y = 3.06 \times 10^{-5}$ and $k_z = 3.61 \times 10^{-6}$ N/m. The origin of the coordinate x′y′z′ is at the center of the microfluidic channel.

contact with any objects, the average position of the trapped particle should be at the center of the trap, and the standard deviation of the position signals should be equal to the size of the trapping volume. When the trap volume intercepts an object, the particle will be displaced from the center of the trap, and the accessible volume within the trap is reduced as well. Thus, from the average or standard deviation of position signals, one should be able to identify whether the trap is free in solution or in contact with an object.

Figure 4.6 shows the average position of the particle relative to the center of the trap as the trap scanned across a microfluidic channel in the x' direction. The

scan started at the center of the channel, where the trap was free in solution. At this region, the average position remained zero in all three dimensions. When the trap scanned to both sides, the particle made contact with the channel walls starting at the positions indicated by those two arrows on the average position trace along the X axis. After this position, the average position along the axis X decreased or increased monotonically, which corresponds to the displacement of the particle away from the center of the trap by the channel walls. At the position indicated by the dashed lines where the displacement of the particle reached the maximum, the particle was pushed out of the trap volume completely and the particle was no longer confined by the trap. Beyond this position, the position signal on QPD could not be interpreted correctly since the particle may have gone beyond the linear region of the detector. The distance from the position where the particle made the initial contact with the channel walls to the position where the particle was lost is about 300 nm. This number represents the maximum width of the trapping volume along the X direction. It is much greater than the width of the trapping volume calibrated using Boltzmann statistics since the external force generated by the channel wall can push the particle to a higher energy region in the potential than thermal forces. As we would expect from the ideal case, the average signal on X should remain zero when the trap is at the region between the center of the channel and the initial contact position. However, the average signal on X moved away from zero gradually as the trap approached the initial contact position. This is more irregular for the average signal along the Z direction. This deviation can be attributed to the non-perfect refractive index match between the liquid medium and the PDMS sample. Forward propagating laser light will have significant scattering at the sample surface due to this mismatch. If the sample surface is not regular, for example a corner of the

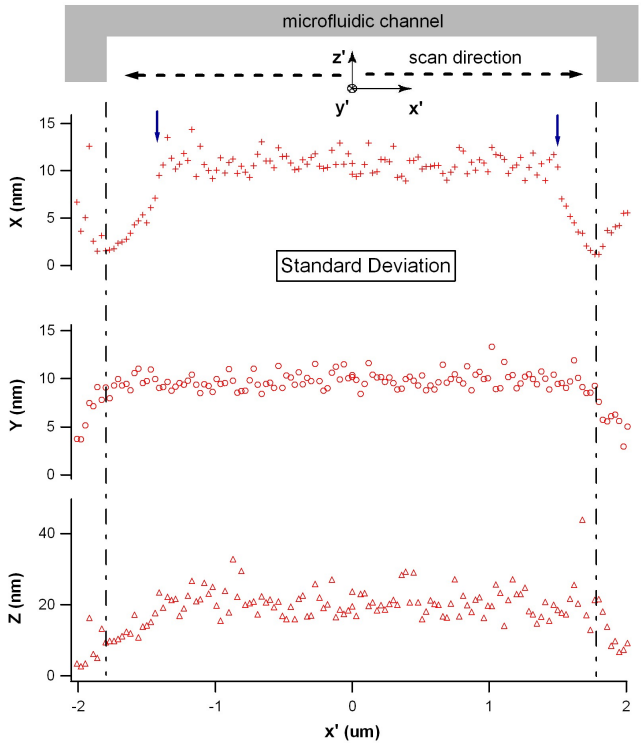

Figure 4.7: Standard deviation of the position signal calculated from the same data used in Figure 4.6.

channel, non-trivial artifacts can be introduced to the position signals. Therefore, for optically inhomogeneous samples, the average position signal would not serve as a reliable indicator for the feedback control.

On the contrary, the standard deviation of the position signal is not sensitive to the inhomogeneous scattering along the light path. In Figure 4.7, standard deviations of position signals in the same experiment as above are shown. At the region between the center of the channel and the initial contact position, the standard deviation along X remained constant with a value of about 10 nm. After the initial contact with the channel walls, the standard deviation along X decreased monotonically until it reached a minimum of about 1.5 nm at the position indicated

by the dashed line. After this position, the particle was pushed out of the trapping volume completely. This minimum value of 1.5 nm corresponds to the resolution limit of the detector. Standard deviations along the Y and Z directions both kept constant values of about 9 nm and 18 nm respectively before the particle was lost, indicating no additional confinement by external objects along these two directions. The standard deviation signals in all three directions clearly showed the constraints coming from the X direction only, which matched the orientation of the channel and the scanning direction. The standard deviation signals are not sensitive to the inhomogeneous optical properties of the environment and serve as robust indicators of contact with objects. In the successive raster scan experiments, standard deviation signals as feedbacks were used.

In the thermal noise imaging mode, the position histogram of the trapped particle should indicate the whole trapping volume if the trap is free in solution. If in contact with any objects, the position histogram will show the accessible volume and should map the surface profile of the objects in contact. Figure 4.8 presents the cross sections of the particle's three dimensional position histogram for a trap free in solution (a) and a trap intercepting a planar surface (b). In Figure 4.8 (a), the position histogram demonstrates the entire trapping volume. It is an ellipsoid with a width of around 150 nm along X and Y, and 300 nm along Z. When the trap intercepted a planar surface along the X direction, its motion along the X direction was confined while motion along the other two directions remained the same. In Figure 4.8 (b), sharp edges are clearly visible along the directions perpendicular to X on both the XY and the XZ cross sections, indicating that the channel was brought into contact with the trap from the right side. The roughness on these edges in the XY and the XZ cross sections is below 20 nm, which is due to the

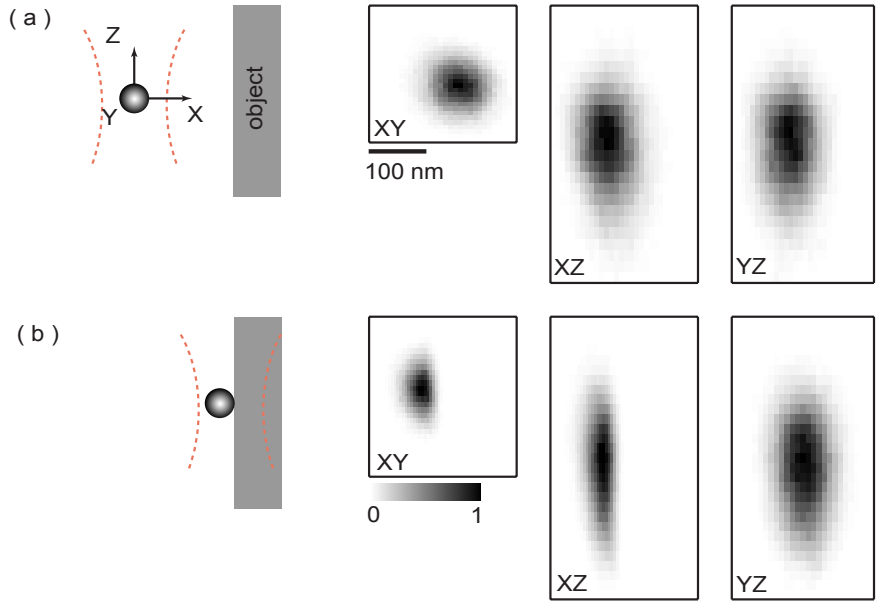

Figure 4.8: Cross sections (at x = 0, y = 0 and z = 0) of a 3D position histogram of a 200 nm trapped particle free in solution (a) and in contact with a planar surface (b). Data was sampled at 100 KHz for 5 seconds. The 3D position histogram is calculated with a bin size of 10 nm. Counts are normalized to the maximal value in each cross section. The force constants of the trap are $k_x = 2.75 \times 10^{-6}$, $k_y = 3.28 \times 10^{-6}$ and $k_z = 7.64 \times 10^{-7}$ N/m respectively.

statistical noise of the position histogram. The surface on the restricted side of the 3D position histogram as indicated by the XY and the XZ cross sections matches very well with the surface of the planar wall. To explore a larger area with TNI, the trap can be scanned in that area and histograms of multiple traps can be combined to produce the thermal noise image. As a demonstration of thermal noise imaging, Figure 4.8 shows how well the thermal noise imaging can be used to image objects with resolutions much higher than light microscopy.

4.2.4 The application to large scale objects

With the implementation of a feedback control system, raster scans can be effectively combined with thermal noise imaging when imaging large scale objects. Figure 4.9 demonstrates a combination of raster scan and local thermal noise imaging on a microfluidic channel. The raster scan was first employed to determine the profile of the channel with a stepsize of 50 nm in all three dimensions with a scan path shown in Figure 4.9 (a). When the standard deviation of the position signal along the X direction was reduced to 60% of its value at the free region, the feedback system decided that the particle encountered an object and would bring the trap to its starting position. Otherwise, the trap would scan up to the pre-chosen boundary before it retracted back to its starting position. In the raster scan, if the particle did not sense any objects in one volume element, a value of 0 was assigned. On the contrary, 1 was assigned to the volume element when the particle sensed the presence of an object. An isosurface with a value of 1 in the scanned volume represents the existing objects in that volume. Figure 4.9 (b) shows the raster scan results of the channel, indicating that the channel has a width of about 4 μm and a depth of 1.6 μm. The resolution in the raster scan is mainly determined by the step size,

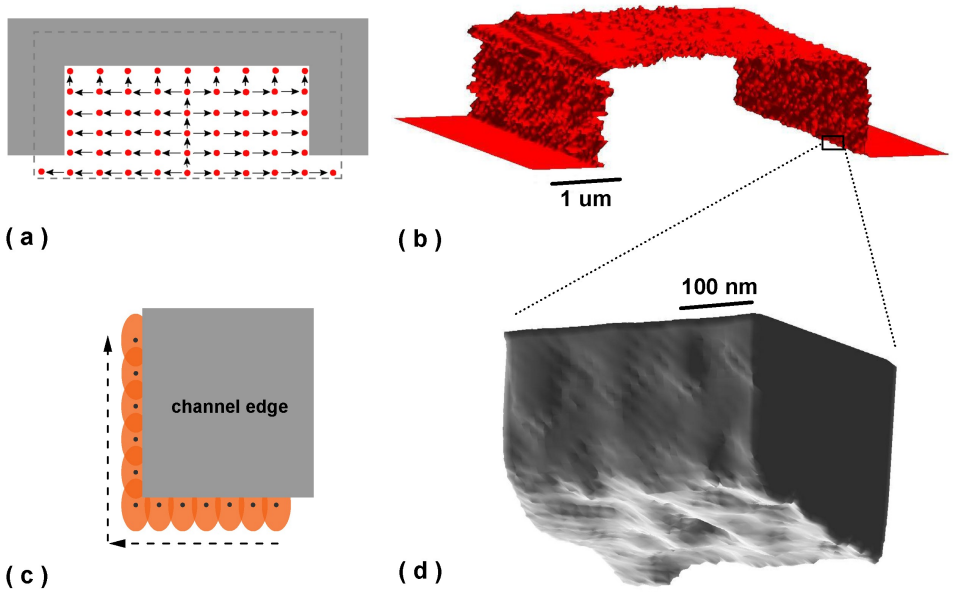

Figure 4.9: Raster scan and TNI schemes and images of a PDMS channel. (a) Scheme of an raster scan; (b) A raster scan image of a microfluidic channel using standard deviation of the position signal as the feedback signal. The particle used was 1 μm in diameter. The stepsize was 50 nm and the data was sampled at 100 KHz for 5 milliseconds at each step. Forces applied on the surface were around 1.4 pN; (c) Scheme of thermal noise imaging; (d) High resolution thermal noise image of an edge at the channel. The size of the particle used was 200 nm in diameter. The stepsize is 80 nm and the data was acquired at 100 KHz for 1 second at each position.

which is about 50 nm. Thermal noise imaging was applied at a small corner indicated by the rectangle following the scan path shown in Figure 4.9 (c). The thermal noise image of that corner is displayed in Figure 4.9 (d).

In the above experiments, the raster scan took about 16 minutes for the predefined volume of $5 \times 3 \times 3$ μm, and the thermal noise imaging on the corner took less than 1 minute. This greatly reduces the imaging time if we are only interested in one small area that can represent the properties of periodic structures. Were thermal noise imaging applied to the whole registered surface of the channel in the predefined volume, it would take about 43 minutes. Combined with raster scanning, the total time it will take to image such a $5 \times 3 \times 3$ μm volume in the channel is 59 minutes. If only thermal noise imaging were applied to the same volume, the total imaging time would be about 2400 minutes. Thus, the combination of raster scan and local thermal noise imaging increases the imaging efficiency by more than 40 times. Of course the imaging efficiency will be different depending on the actual structures of the objects in the volume of interest.

4.2.5 Discussion and summary

The combination of raster scan with local thermal noise imaging greatly improves the imaging efficiency by more than 40 times, which makes imaging large scale objects in three dimensions possible. The efficiency of the raster scan is mainly limited by the step size and the dwelling time at each trap position if standard deviation is used as a feedback signal for optically inhomogeneous materials. Sufficient dwelling time is needed for the particle to explore the accessible volume so that the standard deviation in a free trap and a confined trap can be differentiated. A smaller step size gives better resolution in raster scans but more time is required to complete

the scan. If rough estimates of objects are only needed, doubling the step size can reduce the scanning time by 8 times. However, the step size should be limited to the minimum linear length of the trapping volume so that the particle would not be lost between two successive steps before the feedback control system senses the presence of objects. If inhomogeneous scattering is not a concern in a sample, for example random polymer networks, the average position can be used for feedback control. In this case, the main limiting factor is how fast one can scan the trap. The scan speed is restricted by the maximum trapping force so that the particle would not be lost during the scan. At the typical power of 100 mW [4] used in the experiment, the stiffness along the fast scanning axis is about $k_x = 2.78 \times 10^{-5}$ N/m for a 1 μm polystyrene particle. The maximum trapping force that can be applied to the particle is about 4.2 pN assuming a maximum displacement of 150 nm. This corresponds to a speed of about 500 μm/s estimated by Stoke's law. For this purpose, a bigger particle is better since it experiences a stronger trapping force at the same laser power than smaller particles. One can also increase the laser power to increase the maximum trapping force, but the photodamage to the sample caused by excess laser power should be avoided. Different threshold values of laser power ranging from 40 mW to 160 mW for the 1064 nm wavelength laser have been reported for different living organisms without the loss of vitality [20, 111]. The maximum force applied to the sample should also be optimized without distorting the structure of the soft materials during the scanning.

The efficiency of local thermal noise imaging is limited by the diffusion speed of the particle and the sampling frequency. Since the diffusion constant is inversely proportional to the radius of the particle, a smaller particle is better suited for local

[4] This is the laser power measured right after neutral density filter. We estimate the laser power at the focus spot to be about 17.9 mW.

TNI. In our setup, 100 nm particles can be stably trapped for the purpose of TNI. Sampling frequency is limited to the bandwidth of detector and the digitizer. Our latest developments of a faster position detector should be beneficial to TNI in this case [94].

The resolution of TNI does not solely depend on the size of the particle. It is actually the relative curvature of the particle and the structures that determine its resolution as in any other types of scanning probe microscopies. Particles will always be able to make contact with the surface of the object if they have larger curvatures than those of the objects. In this case, a smaller particle can definitely probe finer structures. However, when the curvature of the probe particle is always larger than those of the objects being probed, for example in the extreme case of a planar surface that has a zero curvature, any size particles can make contact with its surface. The limiting factors on the resolution are mainly the bin size of the histogram and the statistical noise associated with it.

By using forward-scattered and unscattered trapping laser light to detect the particle's position, the photonic force microscope is limited to optically transparent or semi-transparent materials. That is usually the case for soft condensed materials or biological materials. Optical inhomogeneity can be compensated by careful refractive index matching between the medium and the materials. For biological applications in which physiological conditions are needed, index matching is usually not an option. In this case, the standard deviation of the position signal can serve as a robust feedback signal for the raster scan.

Adhesion of the trapped particle to the objects during the scan is usually a concern for the experiments. Although we did not see strong adhesive interactions between carboxylated polystyrene particles and PDMS in our experiments, careful

considerations should be made for other systems to avoid adhesion of probe particles to samples. Possible ways to avoid adhesions involve tuning the ionic strength of the buffer and changing the functional groups on the surface of the particle etc.

In conclusion, the combination of active point-to-point scanning and local thermal noise imaging is an effective strategy to increase the efficiency of the three-dimensional scanning probe microscope without scarifying its high resolution. The development of this method should allow for more advances in the investigations of three-dimensional structures in soft materials.

Chapter 5

Concluding Remarks

Thermal motions of a Brownian particle are not only of fundamental interest but also have practical applications in research such as probing the viscoelasticity of complex fluids (microrheology) and spatial imaging of three-dimensional porous materials (thermal noise imaging) etc.. When implemented with high spatiotemporal resolution detectors, the photonic force microscope provides a great tool for detecting and controlling the Brownian motion of microscopic particles.

The development of the novel detector with separate single photodiodes circumvents the bandwidth limits of the conventional position-sensitive quadrant photodiode and increases the temporal resolution of the photonic force microscope more than one order of magnitude. This development facilitates the studies of the fundamental physics of Brownian motion on a single particle at short time scales which were not possible before. The inertia effect of fluid is shown with polystyrene particles of different sizes, whose time evolutions of mean square displacements are determined by only one single parameter – the characteristic time scale of τ_f. The particle's inertia effect on Brownian motion has been clearly shown for 2.5 μm silica

and polystyrene particles as their digression on MSD becomes more prominent at the time scale around τ_p. The continuum hydrodynamic theory on Brownian motion has been verified down to time scales shorter than τ_p. The velocity autocorrelation function of a single Brownian particle is obtained for the first time and has been found to agree with the theory very well.

In general, the combination of high temporal and spatial resolution in observing Brownian motion has many applications in the study of biological processes as well. One example is protein folding, where fast events occur on tens of nanosecond time and angstrom length scales. Another example is the study of Brownian motion in confined geometries, such as the motions of particles in a living cell, which will help us understand how transport occurs within the crowded cytoplasm of living cells. Finally, the thermal motion of a particle bounded to a single molecular motor has been used to investigate its mechanical properties. Using a fast position detector, one can study the motion of molecular motors on much faster time scales with higher spatial resolution which may reveal details about the conformational changes that take place when chemical energy is converted into mechanical work.

The application of Brownian motion for nanometer spatial imaging in three dimensions has achieved great success in soft materials. The combination of raster scanning and local thermal noise imaging has greatly improved the efficiency of thermal noise imaging by more than 40 times. We thus establish a method of large scale scanning with nanometer resolution in three-dimensional scanning probe microscopy, which should permit wider applications of thermal noise imaging in the studies of fundamental problems in soft condensed materials and biological systems.

Bibliography

[1] T.H. Maiman, Nature **187**, 493(1960). *Stimulated optical radiation in ruby*

[2] C.H. Townes, Oxford, U.K.:Oxford Univ. Press (1999). *How the laser happened*

[3] A. Ashkin, IEEE J. Sel. Top. Quantum Electron. **6**, 841(2000). *History of optical trapping and manipulation of small-neutral particle, atoms and molecules*

[4] A. Ashkin, Phys. Rev. Lett. **24**, 156(1970). *Acceleration and trapping of particles by radiation pressure*

[5] A. Ashkin and J.M. Dziedzic, Appl. Phys. Lett. **19**, 283(1971). *Optical levitation by radiation pressure*

[6] A. Ashkin and J.M. Dziedzic, Appl. Phys. Lett. **24**, 586(1974). *Stability of optical levitation by radiation pressure*

[7] A. Ashkin and J.M. Dziedzic, Appl. Phys. Lett. **28**, 333(1976). *Optical levitation in high vacuum*

[8] A. Ashkin and J.M. Dziedzic, Appl. Phys. Lett. **30**, 202(1977). *Feedback stabilization of optically levitated particles*

[9] A. Ashkin, J.M. Dziedzic, J.E. Bjorkholm and S. Chu, Opt. Lett. **11**, 288(1986). *Observation of a single-beam gradient force optical trap for dielectric particles*

[10] B.J. Ackerson and A.H. Chowdhury, Chem. Soc. **83**, 1(1987). *Radiation pressure as a technique for manipulating the particle order in colloidal suspensions*

[11] T.C.B. Schut, G. Hesselink, B.G. de Grooth and J. Greve, Cytometry **12**, 479(1991). *Experimental and theorectical investigations on the validity of the geometrical optics model for calculating the stability of optical traps*

[12] S. Sato, M. Ohyumi, H. Shibata, H. Inaba and Y. Ogawa, Opt. Lett. **16**, 282(1991). *Optical trapping of small particles using a 1.3-μm compact InGaAsP diode laser*

[13] K. Visscher and G.J. Brakenhoff, Cytometry **12**, 486(1991). *Single beam optical trapping integrated in a confocal microscope for biological applications*

[14] J.Y. Walz and D.C. Prieve, Langmuir **8**, 3073(1992). *Prediction and measurement of the optical trapping forces on a microscopic dielectric sphere*

[15] H. Misawa, K. Sasaki, M. Koshioka, N. Kitamura and H. Masuhara, Macromolecules **26**, 282(1993). *Laser manipulation and assembling of polymer latex particles in solution*

[16] L.P. Ghislain, N.A. Switz and W.W. Webb, Rev. Sci. Instrum. **65**, 2762(1994). *Measurement of small forces using an optical trap*

[17] W.H. Wright, G.J. Sonek and M.W. Berns, Appl. Phys. Lett. **63**, 715(1993). *Radiation trapping forces on microspheres with optical tweezers*

[18] K. Sasaki, M. Koshioka, H. Misawa, N. Kitamura and H. Masuhara, Appl. Phys. Lett. **60**, 807(1992). *Optical trapping of a metal particle and a water droplet by a scanning laser beam*

[19] A. Hirai, H. Monjushiro and H. Watarai, Langmuir **12**, 5570(1996). *Laser photophoresis of a single droplet in oil in water emulsions*

[20] A. Ashkin, J.M. Dziedzic and T. Yamane, Nature **330**, 769(1987). *Optical trapping and manipulation of single cells using infrared laser beams*

[21] A. Ashkin and J.M. Dziedzic, Science **235**, 1517(1987). *Optical trapping and manipulation of viruses and bacteria*

[22] K. Visscher, S.P. Gross and S.M. Block, IEEE J. Sel. Top. Quantum Electron. **2**, 1066(1996). *Optical trapping and manipulation of viruses and bacteria*

[23] G.J. Brouhard, H.T. Schek and A.J. Hunt, IEEE Trans. Biomed. Eng. **50**, 121(2003). *Advanced optical tweezers for the study of cellular and molecular biomechanics*

[24] R.Nambiar and J.C. Meiners, Opt. Lett. **27**, 836(2002). *Fast position measurements with scanning line optical tweezers*

[25] E.R. Dufresne and D.G. Grier, Rev. Sci. Instrum. **69**, 1974(1998). *Optical tweezer array and optical substrates created with diffractive optics*

[26] E.R. Dufresne, G.C. Spalding, M.T. Dearing, G.A. Sheetz and D.G. Grier, Rev. Sci. Instrum. **72**, 1810(2001). *Computer-generated holographic optical tweezer arrays*

[27] V. Garces-Chavez, D. McGloin, H. Melville, W. Sibbett and K. Dholakia, Nature **419**, 145(2002). *Simultaneous micromanipulation in multiple planes using a self-reconstruction light beam*

[28] T. Cizmar, V. Kollarova, X. Tsampoula, F. Gunn-Moore, W. Sibbett, Z. Bouchal and K. Dholakia, Opt. Exp. **16**, 14024(2008). *Generation of multiple Bessel beams for a biophotonics workstation*

[29] S.A. Tatarkova, W. Sibbett and K. Dholakia, Phys. Rev. Lett. **91**, 038101(2003). *Brownian particle in an optical potential of the washboard type*

[30] M. Brunner and C. Bechinger, Phys. Rev. Lett. **88**, 248302(2002). *Phase behavior of colloidal molecular crystals on triangular light lattices*

[31] M.K. Cheezum, W.F. Walker and W.H. Guilford Biophys. J. **81**, 2378(2001). *Quantitative comparison of algorithms for tracking single fluorescent particles*

[32] M. Speidel, A. Jonas and E.-L. Florin, Opt. Lett. **28**, 69(2003). *Three-dimensional tracking of fluorescent nanoparticles with subnanometer precision by use of off-focus imaging*

[33] K. Svoboda, C.F. Schmidt, B.J. Schnapp and S.M. Block, Nature **365**, 721(1993). *Direct observation of kinesin stepping by optical trapping interferometry*

[34] F. Gittes and C.F. Schmidt, Opt. Lett. **23**, 7(1998). *Interference model for back-focal-plane displacement detection in optical tweezers*

[35] A. Pralle, M. Prummer, E.-L. Florin, E.H.K. Stelzer and J.H.K Horber, Microsc. Res. Tech. **44**, 378(1999). *Three-dimensional high-resolution particle tracking for optical tweezers by forward scattered light*

[36] S.C. Kuo and M.P. Sheetz, Science **260**, 232(1993). *Force of single kinesin molecules measured with optical tweezers*

[37] J.T. Finer, R.M. Simmons and J.A. Spudich, Nature **368**, 113(1994). *Single myosin molecule mechanics - piconewton forces and nanometer steps*

[38] K. Visscher, M.J. Schnitzer and S.M. Block, Nature **400**, 184(1999). *Single kinesin molecules studied with a molecular force clamp*

[39] J.E. Molloy, J.E. Burns, J. Kendrick-Jones, R.T. Tregear and D.C.S. White, Nature **378**, 209(1995). *Movement and force produced by a single myosin head*

[40] M.D. Wang, M.J. Schnitzer, H. Yin, R. Landick, J. Gelles and S.M. Block, Science **282**, 902(1998). *Force and velocity measured for single molecules of RNA polymerase*

[41] L. Bai, T.J. Santangelo and M.D. Wang, Annu. Rev. Biophys. Biomol. Struc. **35**, 343(2006). *Single-molecule analysis of RNA polymerase transcription*

[42] K.M. Herbert, W.J. Greenleaf and S.M. Block, Annu. Rev. Biochem. **77**, 149(2008). *Single-molecule studies of RNA polymerase: motoring along*

[43] L. Tskhovrebova, J. Trinick, J.A. Sleep and R.M. Simmons, Nature **387**, 308(1997). *Elasticity and unfolding of single molecules of the giant muscle protein titin*

[44] M.S.Z. Kellermayer, S.B. Smith, C. Bustamante and H.L. Granzier, Elastic Filaments of the Cell **481**, 111(2000). *Mechanical manipulation of single titin molecules with laser tweezers*

[45] J. Liphardt, B. Onoa, S.B. Smith, I. Tinoco and C. Bustamante, Science **292**, 733(2001). *Reversible unfolding of single RNA molecules by mechanical force*

[46] E.A. Abbondanzieri, W.J. Greenleaf, J.W. Shaevitz, R. Landick and S.M. Block, Nature **438**, 460(2005). *Direct observation of base-pair stepping by RNA polymerase*

[47] J.D. Wen, L. Lancaster, C. Hodges, A.C. Zeri, S.H. Yoshimura, H.F. Noller, C. Bustamante and I. Tinoco, Nature **452**, 598(2008). *Following translation by single ribosomes one codon at a time*

[48] G.M. Wang, E.M. Sevick, E. Mittag, D.J. Searles and D.J. Evans, Phys. Rev. Lett. **89**, 050601(2002). *Experimental demonstration of violation of the second law of thermodynamics*

[49] J. Liphardt, S. Dumont, S.B. Smith, I. Tinoco and C. Bustamante, Science **296**, 1832(2002). *Equilibrium information from nonequilibrium measurements in an experimental test of Jarzynski's equality*

[50] E.H. Trepagnier, C. Jarzynski, F. Ritort, G.E. Crooks, C. Bustamante and J. Liphardt, Proc. Natl. Acad. Sci. USA **101**, 15038(2004). *Experimental test of Hatano and Sasa's nonequilibrium steady-state equality*

[51] D. Collin, F. Ritort, C. Jarzynski, S.B. Smith, I. Tinoco and C. Bustamante, Nature **437**, 231(2005). *Verification of the Crooks fluctuation theorem and recovery of RNA folding free energies*

[52] M.T. Woodside, P.C. Anthony, W.M. Behnke-Parks, K. Larizadeh, D. Herschlag and S.M. Block, Science **314**, 1001(2006). *Direct measurement of the full sequence-depedent folding landscape of a nucleic acid*

[53] E.-L Florin, A. Pralle, E.H.K. Stelzer, Appl. Phys. A **6**, s75(1998). *Photonic force microscope calibration by thermal noise analysis*

[54] S. Jeney, E.H.K. Stelzer, H. Grubmuller and E.-L. Florin, Chem. Phys. Chem. **5**, 1150(2004). *Mechanical properties of single motor molecules studies by three-dimensional thermal force probing in optical tweezers*

[55] C. Tischer, S. Altmann, S. Fisinger, J.K.H. Horber, E.H.K. Stelzer and E.-L. Florin Appl. Phys. Lett. **79**, 3878(2001). *Three-dimensional thermal noise imaging*

[56] A.Ashkin, Biophys. J. **61**, 569(1992). *Forces of a single-beam gradient laser trap on a dielectric sphere in the ray optics regime*

[57] Y. Harada and T. Asakura, Opt. Comm. **124**, 529(1996). *Radiation forces on a dielectric sphere in the Rayleigh scattering regime*

[58] M. Kerker, Academic, New York(1969). *The scattering of light and other electromagnetic radiation*

[59] K.C. Neuman and S.M. Block, Rev. Sci. Instrum. **75**, 2787(2004). *Optical trapping*

[60] A. Rohrbach and E.H.K. Stelzer, J. Opt. Soc. Am. A **18**, 839(2001). *Optical trapping of dielectric particles in arbitrary fields*

[61] V.P. Zharov, T.V. Malinsky and R.C. Kurten, J. Phys. D **38**, 2662(2005). *Photoacoustic tweezers with a pulsed laser: theory and experiments*

[62] S. Hell, G. Reiner, C. Cremer and E.H.K. Stelzer, J. Microscopy-Oxford **169**, 391(1993). *Aberrations in confocal fluorescence microscopy induced by mismatches in refractive index*

[63] B.E.A. Saleh and M.C. Teich, New York:John Wiley & Sons(1991). *Photonics*

[64] C.W. Wang and G.E. Uhlenbeck, in Selected Papers on Noise and Stochastic Processes (ed. Wax, N.), 113 (Dover, New York, 1954).

[65] P.Y. Wu*, R.X. Huang*, C. Tischer, A. Jonas and E.-L. Florin, submitted to Phys. Rev. Lett. (2008). *Direct measurement of the nonconservative force field generated by optical tweezers*

[66] C. Tischer, A. Pralle and E.-L Florin, Microscopy and Microanalysis **10**, 425(2004). *Determination and correctio of position detection nonlinearty in single particle tracking and three-dimensional scanning probe microscopy*

[67] J. Happel and H. Brenner, Noordhoff, Leyden (1973). *Low Reynolds number hydrodynamics*

[68] H. Faxen, Ph.D. thesis, Uppsala (1921).

[69] E. Frey and K. Kroy, Ann. Phys. **14**, 20(2005). *Brownian motion: a paradigm of soft matter and biological physics*

[70] R.M. Mazo, Clarendon Press, Oxford(2005). *Brownian motion: fluctuations, dynamics and applications*

[71] R. Brown, 1828.*A brief account of microscopical observations made in the months of June, July and August, 1827 on the particles contained in the pollen of plants;and on the general existence of active molecules in organic and inorganic bodies*

[72] A. Einstein, Ann. Phys. **17**, 549(1995).

[73] J. Perrin, C. R. Acad. Sci. Paris **147**, 475(1908a).

[74] J. Perrin, C. R. Acad. Sci. Paris **147**, 530(1908b).

[75] T.G. Mason, K. Ganesan, J.H. vanZanten, D. Wirtz and S.C. Kuo, Phys. Rev. Lett. **79**, 3282(1997). *Particle tracking microrheology of complex fluids*

[76] M. Smoluchowski, Ann. D. Phys. **21**, 756(1906).

[77] P. Langevin, C. R. Acad. Sci. Paris **146**, 530(1908).

[78] B.J. Alder and T.E. Wainwright, Phys. Rev. Lett. **18**, 988(1967). *Velocity autocorrelations for hard spheres*

[79] B.J. Alder and T.E. Wainwright, Phys. Rev. A **1**, 18(1970). *Decay of the velocity autocorrelation function*

[80] V. Vladimirsky and Ya Terletzky, Zhur. Eksp Teor. Fiz. **50**, 1084(1945).

[81] E.J. Hinch, J. Fluid Mech. **72**, 499(1975). *Application of the Langevin equation to fluid suspensions*

[82] D.J. Acheson, Oxford Applied Mathematics and Computing Science Series, Oxford University Press, (1990). *Elementary fluid dynamics*

[83] T.B. Liverpool and F.C. MacKintosh, Phys. Rev. Lett. **95**, 208303(2005). *Inertial effects in the response of viscous and viscoelastic fluids*

[84] S. Chandrasekhar, Rev. Mod. Phys. **15**, 1(1943). *Stochastic problems in physics and astronomy*

[85] J. Boussinesq, *Theorie analytique de la chaleur*, Paris (1903).

[86] L.D. Landau and E.M. Lifshitz, *Theorie analytique de la chaleur*, Pergamon, New York (1959).

[87] R. Zwanzig and M. Bixon, J. Fluid Mech. **69**, 21 (1975). *Compressibility effects in the hydrodynamic theory of Brownian motion*

[88] H.J.H. Clercx and P.P.J.M. Schram, Phys. Rev. A **46**, 1942(1992). *Brownian particles in shear flow and harmonic potentials: A study of long-time tails*

[89] D.J. Pine, D.A. Weitz, P.M. Chaikin and E. Herbolzheimer, Phys. Rev. Lett. **60**, 1134(1988). *Diffusing-wave spectroscopy*

[90] J.X. Zhu, D.J. Durian, J. Muller, D.A. Weitz and D.J. Pine, Phys. Rev. Lett. **68**, 2559(1992). *Scaling of transient hydrodynamic interactions in concentrated suspensions*

[91] M.H. Kao, A.G. Yodh and D.J. Pine, Phys. Rev. Lett. **70**, 242(1993). *Observation of Brownian motion on the time scale of hydrodynamic interactions*

[92] S. Henderson, S. Mitchell and P. Barlett, Phys. Rev. Lett. **88**, 088302(2002). *Propagation of hydrodynamic interactions in colloidal suspensions*

[93] B. Lukić, S. Jeney, C. Tischer, A.J. Kulik, L. Forró and E.-L. Florin, Phys. Rev. Lett. **95**, 160601(2005). *Direct observation of nondiffusive motion of a Brownian particle*

[94] I. Chavez, R.X. Huang, K. Henderson, E.-L. Florin and M.G. Raizen, Rev. Sci. Instrum. **79**, 1(2008). *Development of a fast position-sensitive laser beam detector*

[95] G. Binnig, C.F. Quate and C. Gerber, Phys. Rev. Lett. **56**, 930(1986). *Atomic force microscope*

[96] J.K.H. Horber and M.J. Miles, Science **302**, 1002(2004). *Scanning probe evolution in biology*

[97] F.J. Giessibl, Science **267**, 5194(1995). *Resolution of the silicon (111)-(7×7) surface by atomic force microscopy*

[98] H.G. Hansma and J.H. Hoh, Annu. Rev. Biophys. Biomol. Struct. **23**, 115(1994). *Biomolecular Imaging with the atomic force microscope*

[99] M. Ternes, C.P. Lutz, C.F. Hirjibehedin, F.J. Giessibl and A.J. Heinrich, Science **319**, 1066(2008). *The force needed to move an atom on a surface*

[100] L. Malmqvist and H.M. Hertz, Opt. Commun. **94**, 930(1992). *Trapped particle optical microscopy*

[101] L.P. Ghislain and W.W. Webb, Opt. Lett. **18**, 1678(1993). *Scanning-force microscope based on an optical trap*

[102] L. Malmqvist and H.M. Hertz, Opt. Lett. **19**, 853(1994). *Two-color trapped-particle optical microscopy*

[103] S. Kawata, Y. Inouye and T. Sugiura, Jpn. J. Appl. Phys. **33**, L1725(1994). *Near-field scanning optical microscope with a laser trapped probe*

[104] E.-L. Florin, J.K.H. Horber and E.H.K. Stelzer, Appl. Phys. Lett. **69**, 446(1996). *High-resolution axial and lateral position sensing using two-photon excitation of fluorophores by a continuous-wave Nd:YAG laser*

[105] E.-L. Florin, A. Pralle, J.K.H. Horber and E.H.K. Stelzer, J. Struc. Bio. **119**, 202(1997). *Photonic force microscope based on optical tweezers and two-photon excitation for biological applications*

[106] M.E.J. Friese, A.G. Truscott, H. Rubinsz, Appl. Phys. Lett. **69**, 446(1996). *High-resolution axial and lateral position sensing using two-photon excitation of fluorophores by a continuous-wave Nd:YAG laser*

[107] E.-L. Florin, J.K.H. Horber and E.H.K Stelzer, US and German patent application (2000). *Thermal noise imaging*

[108] C. Tischer, Ph.D. thesis (2005).

[109] K. Kroy, Curr. Opin. in Coll. and Inter. Sci. **11**, 56(2006). *Elasticity, dynamics and relaxation in biopolymer networks*

[110] K. Kroy and E. Frey, Phys. Rev. Lett. **77**, 306(1996). *Force-extension relation and plateau modulus for wormlike chains*

[111] K. Neuman, E.H. Chadd, G.F. Liou, K. Bergman and S.M. Block, Biophys. J. **77**, 2656(1999). *Characterization of photodamage to Escherichia coli in optical traps*

Vita

Rongxin Huang was born on December 2, 1978 in Xiamen, Fujian, China to Bingshan Huang and Yibin Huang. He graduated from Jimei High School, Xiamen in July 1997. He received the Bachelor of Science degree in Materials Science and Engineering (minor in Materials Physics) in June 2002 from the University of Science and Technology of China, Hefei after completing the five-year undergraduate program. In the fall of 2002 he enrolled in the graduate program of the physics department at the University of Texas at Austin. In January of 2004 he became the first graduate student of the biophysics group led by Prof. Ernst-Ludwig Florin at the Center for Nonlinear Dynamics where he has performed experiments studying Brownian motion at fast time scales and three-dimensional thermal noise imaging.

Permanent Address: JiMeiQu HouXiZhen LunShangCun DaSheLu 50

Xiamen, Fujian 361024, P. R. China

This dissertation was typeset with LaTeX 2_ε[1] by the author.

[1] LaTeX 2_ε is an extension of LaTeX. LaTeX is a collection of macros for TeX. TeX is a trademark of the American Mathematical Society. The macros used in formatting this dissertation were written by Dinesh Das, Department of Computer Sciences, The University of Texas at Austin, and extended by Bert Kay, James A. Bednar, and Ayman El-Khashab.